# Combining point cloud and surface methods for modeling partial shading impacts of trees on urban solar irradiance

Energy & Buildings 298 (2023) 113420

Contents lists available at ScienceDirect

Energy & Buildings

journal homepage: www.elsevier.com/locate/enb

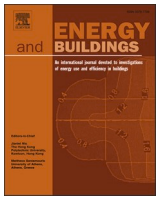

# Combining point cloud and surface methods for modeling partial shading impacts of trees on urban solar irradiance

B. Tian *, R.C.G.M. Loonen, J.L.M. Hensen

*Building Physics and Services, Eindhoven University of Technology, Postbus 513, 5600 MB Eindhoven, The Netherlands*

ARTICLE INFO

*Keywords:*
Fusion model
Solar irradiance
Tree shading
Dynamic graph CNN

ABSTRACT

Although trees and urban vegetation have a significant influence on solar irradiation in the built environment, their impact on daylight and energy consumption is often not considered in building performance and urban environment simulation studies. This paper presents a novel method for comprehensive solar irradiance assessment that considers the dynamic partial shading impacts from trees. The proposed method takes urban point clouds as input and consists of three subsequent steps: (a) DGCNN-based segmentation, (b) fusion model generation, (c) matrix-based irradiance calculation. The method is validated by comparing model outputs with field measurement data, and an inter-model comparison with eleven state-of-the-art tree shading modeling approaches. Analyses carried out on daily and long-term basis show that the proposed fusion model can significantly reduce simulation errors compared to alternative approaches, while limiting the required input data to a minimum. The primary source of uncertainty stems from mismatches between tree morphology in the fusion model and reality, attributable to phenological growth and seasonal variations.

## 1. Introduction

Trees form an essential part of the built environment, offering a myriad of ecological, environmental, psychological, and economic advantages to urban residents [1,2]. Numerous studies concerned with building energy performance simulation [3–6] have demonstrated that trees have significant shading effect on solar radiation and cooling effect within urban settings, substantially contributing to decreased energy consumption in buildings. Furthermore, incorporating systematic tree planning into energy-efficient and thermal-visual comfort strategies can bolster sustainable building and urban design practices [7–9].

Although the aforementioned benefits of trees are well-established, they can also pose substantial challenges to solar energy harvesting in urban environments [10,11]. Tree canopies can block both direct solar radiation and diffuse sky radiation, frequently leading to a considerable reduction in the plane-of-array (POA) irradiance received by photovoltaic (PV) systems, thus resulting in non-optimal operating conditions.

Besides the reduction of POA irradiance, dynamic partial shading caused by trees on PV surfaces can lead to cell-level or module-level mismatch issues and hot spot heating. These factors contribute to further energy loss [12–15] and may even aggravate the degradation of the PV modules [16]. Studies by e.g. Tooke et al. and Fogl et al. [17–20] have found that partial shading effects from trees can significantly reduce rooftop PV production. Consequently, accurate modeling of solar irradiance potential under dynamic shading impacts from trees is crucial for practitioners in order to provide energy yield guarantees for PV systems, make informed decisions in sustainable building design, and manage urban renewable resources effectively.

The state-of-the-art methods that account for tree shading impacts on solar irradiance potential can be broadly categorized into two distinct phases: geometric model generation and irradiance calculation. Geometric model generation refers to the definition of the morphology and dimensions of trees. Irradiance calculation, on the other hand, refers to applying a predefined geometric model of trees to a specific simulation method, which facilitates the quantification of the shading effects induced by trees.

### 1.1. Literature review

The available methods to define the geometric characteristics of trees can be broadly classified into 2D methods based on photographic

*Abbreviations:* BPS, Building performance simulation; BIPV, Building-integrated PV; DGCNN, Dynamic graph convolutional neural networks; GPS, Global Positioning System; HDR, High dynamic range; IQR, Interquartile range; KNN, K-nearest neighbor; LiDAR, Light detection and ranging; NREL, National Renewable Energy Laboratory; POA, Plane-of-array; PV, Photovoltaic; SVM, Support vector machine.

* Corresponding author.
*E-mail address:* b.tian@tue.nl (B. Tian).

https://doi.org/10.1016/j.enbuild.2023.113420
Received 31 May 2023; Received in revised form 14 July 2023; Accepted 1 August 2023
Available online 23 August 2023

**Symbol list**

| | |
|---|---|
| $Abs\_e$ | Cumulative absolute error [Wh/m$^2$] |
| $Avg\ F1$ | Averaged F1 score [Pct] |
| $DC$ | Daylight coefficient [-] |
| $DC_{mtx}$ | Daylight coefficient matrix [-] |
| $E_{mtx\_dif}$ | Sky diffuse irradiance matrix [-] |
| $E_{mtx\_dif\_without\_tree}$ | Sky diffuse irradiance matrix without tree shading impacts [-] |
| $E_{mtx\_dir}$ | Solar direct irradiance matrix [-] |
| $E_{mtx\_dir\_without\_tree}$ | Solar direct irradiance matrix without tree shading impacts [-] |
| $E_{incident}$ | Incident irradiance [W/m$^2$] |
| $FN$ | False negative [-] |
| $FP$ | False positive [-] |
| $G_{cumulative}$ | Cumulative irradiation [Wh/m$^2$] |
| $G_{dif}$ | Sky diffuse radiance [W/m$^2$] |
| $G_{dir}$ | Solar direct radiance [W/m$^2$] |
| $G_{extraterrestrial}$ | Extraterrestrial solar irradiation [Wh/m$^2$] |
| $GHI$ | Global horizontal irradiation [Wh/m$^2$] |
| $G_{mtx\_dif}$ | Sky diffuse radiance matrix [-] |
| $G_{mtx\_dir}$ | Solar direct radiance matrix [-] |
| $K_T$ | Sky clearness index [-] |
| $N$ | Number of data points [-] |
| $OA$ | Overall accuracy [Pct] |
| $Rel\_e$ | Cumulative relative error [Pct] |
| $RMSE$ | Root mean squared error [W/m$^2$] |
| $SEF$ | Small error fraction [Pct] |
| $TSR$ | Tree shading ratio [-] |
| $TSR_{mtx}$ | Tree shading ratio matrix [-] |
| $T$ | Timestep [s] |
| $TN$ | True negative [-] |
| $TP$ | True positive [-] |

imagery and 3D methods based on computer modeling.

#### 1.1.1. 2D imagery methods

2D on-site photography techniques are widely used methods for describing tree geometries in daylight and irradiance studies, for their positive features in terms of user-friendliness, affordability, and comprehensive hemispherical coverage [21]. 2D hemispherical imagery is utilized by several studies to model tree daylight permeability [22–24]. This method has also been applied to calculate leaf gap fraction [25] and tree shade coverage [26] that are vital for urban solar irradiance calculation. Furthermore, High Dynamic Range (HDR) techniques can enhance the quality of hemispherical imagery. Balakrishnan and Jakubiec [27] employed HDR photography to determine transmittance percentages and gap fractions of trees. A main drawback of the use of on-site photography techniques in large-scale or complex environmental simulations pertains to the massive data collection requirements.

#### 1.1.2. 3D computer modeling methods

3D computer modeling offers an intuitive method for generating 3D representations of trees. Creating these models requires assumptions about trees' morphological and optical characteristics. Generally, 3D tree modeling techniques fall into four categories: (i) modeling trees as opaque solid; (ii) modeling trees as semi-transparent solid; (iii) modeling trees as solid with distributed gaps; (iv) modeling trees as point cloud.

*Modeling trees as opaque solid*. Opaque solid models simplify trees into geometric forms with predefined radii and heights. Past studies have used ellipsoidal, spherical, or cylindrical tree models to assess tree shadow factors [28] and shading impacts on building energy performance [29–31]. Recent advancements in reconstructing tree surfaces from point cloud data [11,32–36] have expanded 3D tree representation possibilities. Dominant reconstruction algorithms in tree shading studies include Delaunay triangulation [37–39], Alpha shape [40], Convex hull [41,42], and Poisson [43].

*Modeling trees as semi-transparent solid.* Semi-transparent solid models address limitations of opaque solid models that cannot model the partly transmitted sunlight by incorporating transmittance properties. Szkordilisz and Kiss [44] modeled trees as spheres with transmittance around 0.12, while Hwang et al. [45,46] used elliptical shapes with transmittance of 0.75 in winter and 0.25 in other months to study tree shading impacts on building energy consumption. Peronato et al. [47] employed the Convex hull algorithm to create semi-transparent tree surfaces to examine solar potential on building façades.

*Modeling trees as solid with distributed gaps.* A recent study by Pan and Jakubiec [2] proposes a method for modeling trees as hemisphere or semi-ellipsoid with randomly distributed gaps in crowns. Dereli et al. [48] also applied tree models with gaps to assess shading impacts on PV energy production. These models are available from the Google SketchUp Warehouse, with adjustable canopy height and diameter to meet the requirements of different simulation cases.

*Modeling trees as point cloud*. Point clouds of trees can be directly used in modeling solar PV potential in urban areas [17–19,49] and on building surfaces [50,51] under tree shading impacts. Bognár et al. [52] proposed a comprehensive point cloud-based method for urban irradiance simulation that accounts for shading impacts from solar obstructions, including trees. Compared to (semi-)solid tree models that tend to simplify the shape of tree canopies, point cloud models preserve more detailed geometric information, such as leaf density and irregular organic shapes.

### 1.2. Irradiance calculation

From the review of tree geometry determination approaches in Section 1.1, we found that 3D tree models offer greater scalability and intuitiveness for shading impact estimation compared to 2D photography methods. Numerous solar irradiance modeling techniques have been developed based on 3D models, with comprehensive reviews provided by Freitas et al. [53] and Jakica [54]. The following brief literature review, however, focuses solely on irradiance simulation methods employed in the tree-related studies presented in Section 1.1. Depending on the handling of geometric models in simulations, irradiance calculation techniques can be categorized into two primary types: rule-based methods and matrix-based methods.

#### 1.2.1. Rule-based method

Rule-based methods are designed to estimate shading impacts by modeling geometric relationships between sensor points, obstructions, and the sun, complemented by empirical models for solar irradiance calculations [53]. Although such methods are efficient and intuitive to use for specific situations, they also have notable limitations. Rule-based methods are primarily suited for simulating irradiance at specific timesteps, but require substantial computational resources for long-term dynamic shading impact analysis, and do not account for environmental reflections. Moreover, these models primarily cater to horizontal or inclined surfaces and struggle to assess shading impacts of trees on vertical surfaces, such as building facades [17–19,49]. Although some advanced rule-based methods [41,50,51] can estimate tree shadows on vertical surfaces, they fail to accurately determine solar penetration through tree canopies and the shading influence on diffuse sky irradiance.

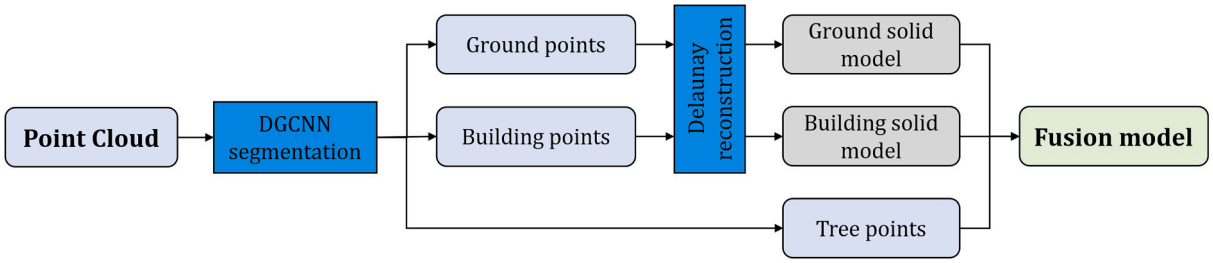


**Fig. 1.** Schematic workflows for fusion model generation.

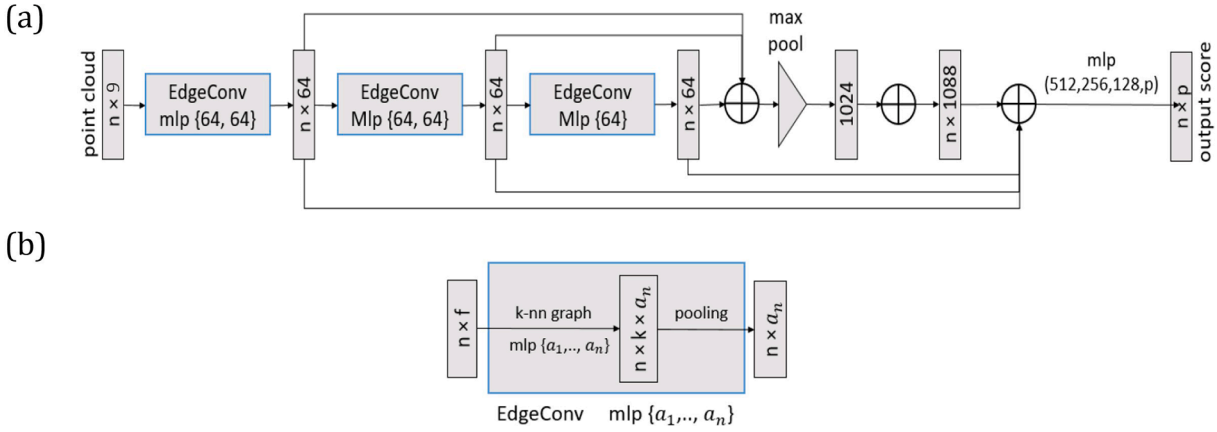


**Fig. 2.** Schematic diagram of DGCNN structure in the present work. (a) Overview of the classification model; (b) EdgeConv module applied to learn local geometric features for each point. .
Adapted from [65]

### 1.2.2. *Matrix-based method*

Contrasting rule-based methods, which rely on empirical formulas for solar irradiance calculations, matrix-based approaches employ sky discretization, dividing the sky hemisphere into equal solid angle segments [55]. This enables representation of sky radiance distribution at each simulation timestep as a sky radiance matrix. Correspondingly, shading impacts of obstructions are considered discretized, estimating shading impacts for each sky segment individually. The cumulative shading impact is then expressed as a daylight coefficient (DC) matrix, denoting the ratio of sky segment's radiance received by a sensor point [56]. Shaded segments correspond to lower DC values, while unshaded segments maintain higher values. Irradiance results under dynamic sky and shading conditions are acquired by multiplying the DC matrix with the sky radiance matrix.

Matrix-based methods are inherently suitable for detailed daylight modeling in 3D urban geometries and expedite long-term simulations [52,57]. Radiance [55] and Pyrano [52], employed by several reviewed studies [2,22,37,40,44,47,52,58], are considered the most representative state-of-the-art matrix-based methods. Previous researches have demonstrated their superior performance in simulating direct and diffuse irradiance under dynamic sky conditions [37,59–62].

The major difference between Radiance and Pyrano lies in their DC matrix calculation approach. Radiance utilizes raytracing, effectively accounting for reflected irradiance from surroundings with solid surface models as necessary input. Such models can be obtained using surface reconstruction techniques [11] and open-access databases [63], facilitating Radiance simulation and reflection assessment with the ground and other buildings. However, as discussed in Section 1.1.2, most tree solid models are highly simplified, deviating from real organic morphologies and limiting Radiance's ability to predict tree shading impacts.

Conversely, Pyrano employs computational point projection for DC matrix calculations [52], using only urban point clouds as input. This method allows to better capture the semi-transparent nature of urban vegetation, by identifying areas of high and low transmittance in the canopy based on local point density. An example of local transmittance modeling for a tree canopy is provided in Appendix A.3. Pyrano assumes that all sky segments contribute to surrounding reflected irradiance on sensor points by specific ratios since the unstructured nature of the point cloud makes it difficult to physically model reflections. This assumption is reasonable for less obstructed scenes with uniform ground-based reflections. However, in complex environments with reflections from diverse obstructing objects, sky segment contributions can vary significantly, leading to inadequate estimations when assuming equivalent contributions. Detailed descriptions of calculation procedures of Radiance and Pyrano are provided in Appendix A.1 and A.2, respectively.

## 1.3. *Research goals*

Building upon the preceding discussion, the two reviewed matrix-based methods, Radiance and Pyrano, have distinct advantages; Radiance excels at assessing environmental reflections but lacks applicability to tree shading studies, while Pyrano effectively models shading and sunlight transmission through trees but struggles with accurately modeling reflections in urban settings. Our aim in this study is to combine their strengths for accurate solar simulation in complex tree-shaded environments, while accounting for surrounding reflections. More specifically, the research goals in this study are twofold:

1. To introduce a novel fusion model for the representation of complex urban environments. Our model combines the solid (surface) modeling of buildings and terrain, while incorporating trees as point clouds. To facilitate the generation of fusion model, we utilize the Dynamic Graph Convolutional Neural Networks (DGCNN) semantic segmentation technique.

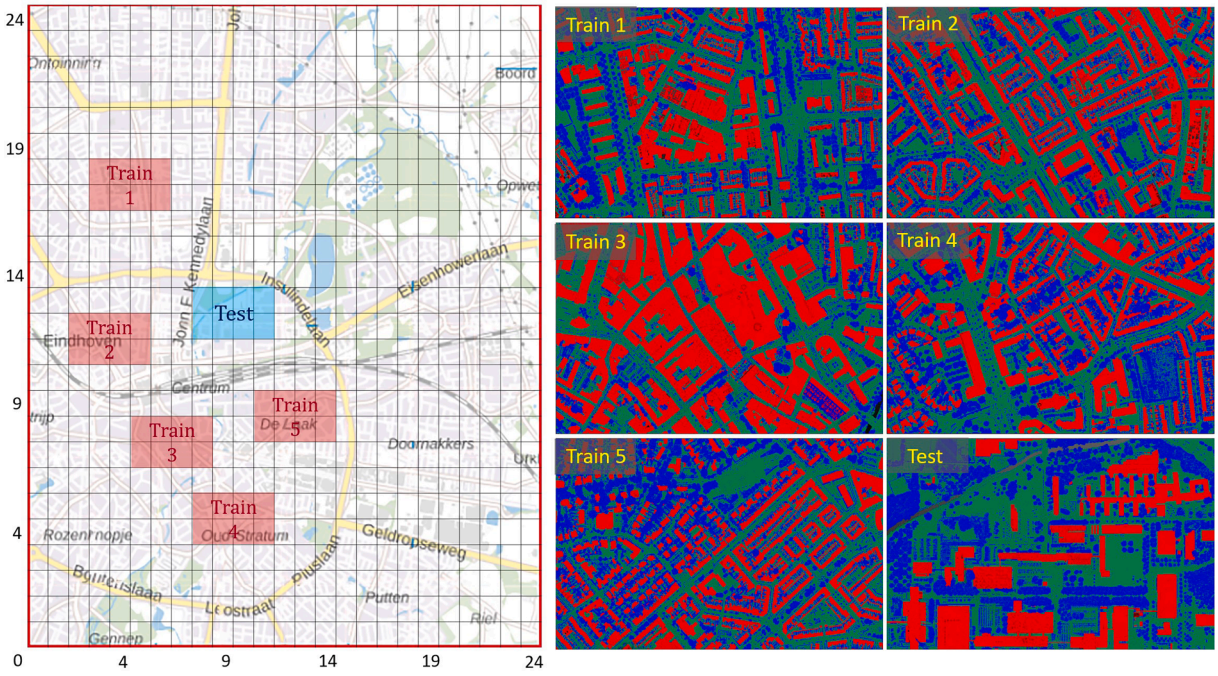


**Fig. 3.** Split LiDAR tile grid and data blocks for DGCNN train and test.

2. To develop and validate an advanced solar irradiance modeling method, built upon the fusion model. By addressing the limitations inherent in existing matrix-based model in accounting for dynamic tree-induced partial shading impacts, we aim to enhance solar irradiance simulation accuracy and minimize associated uncertainties.

The detailed description of our model development procedures will be provided in Section 2. In Section 3, we will present the validation of our proposed fusion modeling method, employing field measurements and inter-model comparisons. Field measurement validation involve comparing fusion model results with measurement data, while the inter-model comparison contrast fusion model results with those from eleven different tree geometric models (reviewed in Section 1.1) in simulations.

## 2. Model development

This section provides details of the proposed hybrid workflow for model generation and solar irradiance modeling. Fig. 1 schematically illustrates the process to generate a fusion model from urban point cloud.

### 2.1. Dynamic graph CNN semantic segmentation

As described in Fig. 1, to generate the fusion model for solar simulation, one of the key steps is to segment the input urban point cloud into three classes: building, ground and trees. Referring to the work by Widyaningrum et al. [64], the present study employs DGCNN for this segmentation task, which is one of the most advanced deep learning methods to perform semantic segmentation tasks within unstructured 3D point clouds [64–66].

The architecture of the DGCNN segmentation model is illustrated in Fig. 2, which uses three sequential EdgeConv layers followed by multiple fully connected 1ayers. The EdgeConv layers are designed to extract local features by constructing dynamic k-nearest neighbor (KNN) graphs. A max pooling operation is implemented after the EdgeConv layers to maintain the model's permutation invariant property while aggregating global features across the point cloud. The fully connected layers will produce class prediction scores for each point. Readers can refer to [65] for a detailed review of DGCNN formulation and calculation.

#### 2.1.1. DGCNN model training

The DGCNN model in the present work is trained by the open-source LiDAR (Light Detection and Ranging) point cloud of Eindhoven, the Netherlands [67]. As shown in Fig. 3, the labelled urban point cloud was divided into a 25 × 25 grid, wherein the red tiles indicate the five datasets for model training, while the blue one indicates the datasets for testing. Besides, in the preparation stage, the LiDAR data is down-sampled to 0.5 m resolution to make the network model more effective in learning the local features among the points.

The points in the LiDAR data contain several feature vectors, among which we have selected nine as the feature set for DGCNN learning: spatial coordinates ($x$, $y$, $z$), color information ($R$, $G$, $B$), and LiDAR collection information ($I$, $R_n$, $N$). Our selection was inspired by the experiments of Widyaningrum et al. [64], where the model showed the best segmentation performance for buildings and trees when the same feature set was used. A NVIDIA GeoForce RTX 3090Ti GPU was used in training and testing stage, and the model used in testing was obtained by choosing the best model after training with 50 epochs.

#### 2.1.2. Evaluation metrics

In the present study, we evaluate the performance of our DGCNN model in segmentation tasks using three metrics: Overall Accuracy, Averaged F1 score, and per-class F1 score.

- Overall Accuracy (*OA*): *OA* is a commonly used metric that measures the proportion of correctly classified points out of the total points in the dataset. It provides a general idea of the model's performance and is easy to compute.
- Per-class F1 score: F1 score is a harmonic mean of recall and precision, used to assess model accuracy (Equation (1)). The formulation of recall and precision are related to the false/true positive rates (*FP*/*TP*) and negative rates (*FN*/*TN*) in the segmentation results on a certain class [68,69], as shown in Equation (2)(3). Recall represents the model's ability to identify all positive samples, while precision quantifies the classifier's accuracy in avoiding false positives.

**Table 1**
DGCNN segmentation results on the testing point cloud tile.

| Metrics | OA (%) | Avg F1 (%) | F1 Score per class (%) | | |
|---|---|---|---|---|---|
| | | | Ground | Buildings | Trees |
| Scores | 94.9 | 93.4 | 97.8 | 95.2 | 87.3 |

$$F1 = \frac{2 \times recall \times precision}{recall + precision} \times 100\% \quad (1)$$

$$recall = \frac{TP}{TP + FN} \quad (2)$$

$$precision = \frac{TP}{TP + FP} \quad (3)$$

- Averaged F1 score (*Avg F1*): *Avg F1* is the mean of the F1 scores computed for each class, thus providing a more comprehensive view of the model's performance.

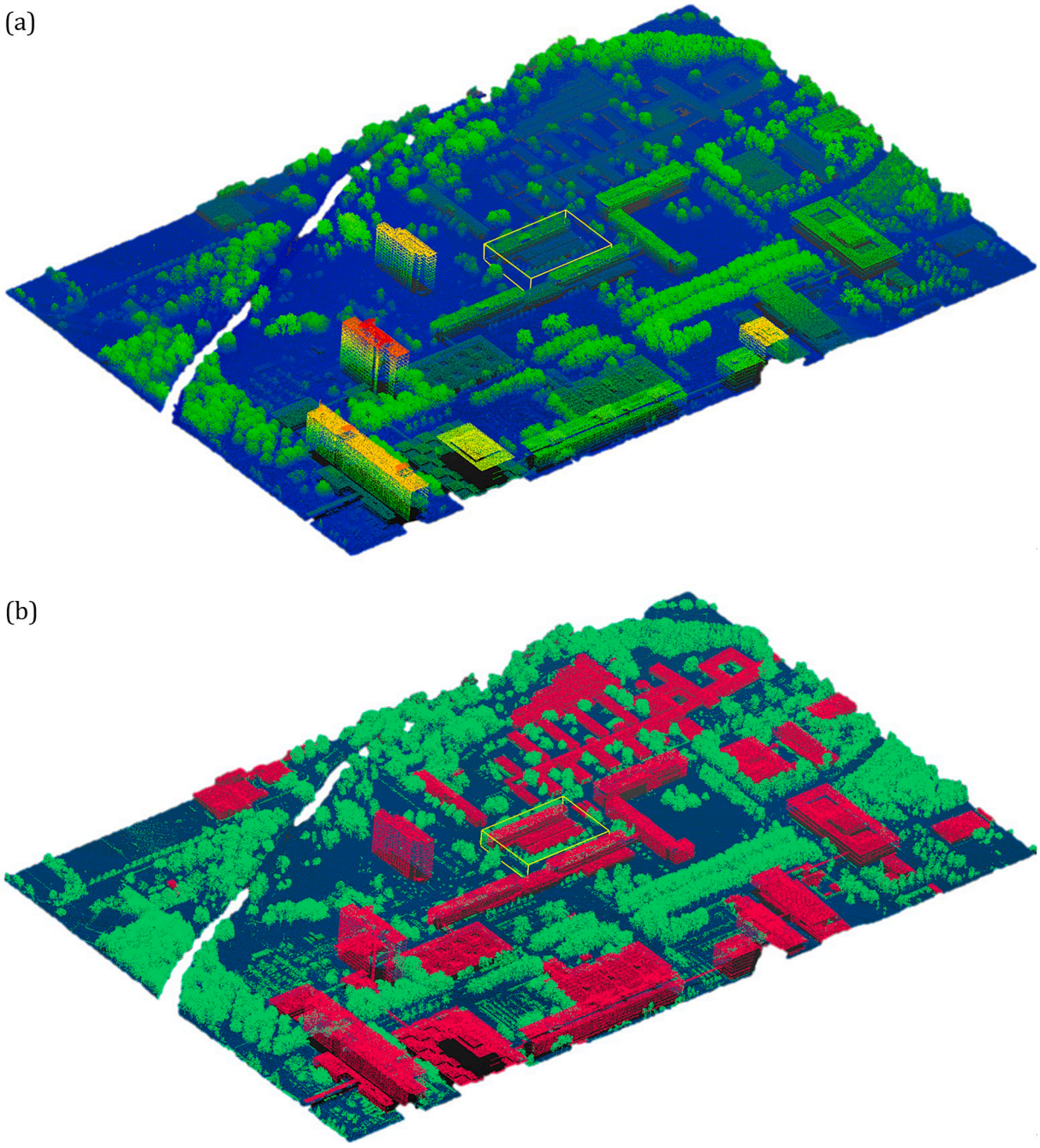


**Fig. 4.** Classification result in the testing point cloud tile, with (a) input point cloud and (b) classified point cloud, where the ground, buildings and trees were colored dark blue, red and green respectively. The yellow bounding box marks the area for validation study in Section 3. (For interpretation of the references to color in this figure legend, the reader is referred to the web version of this article.)

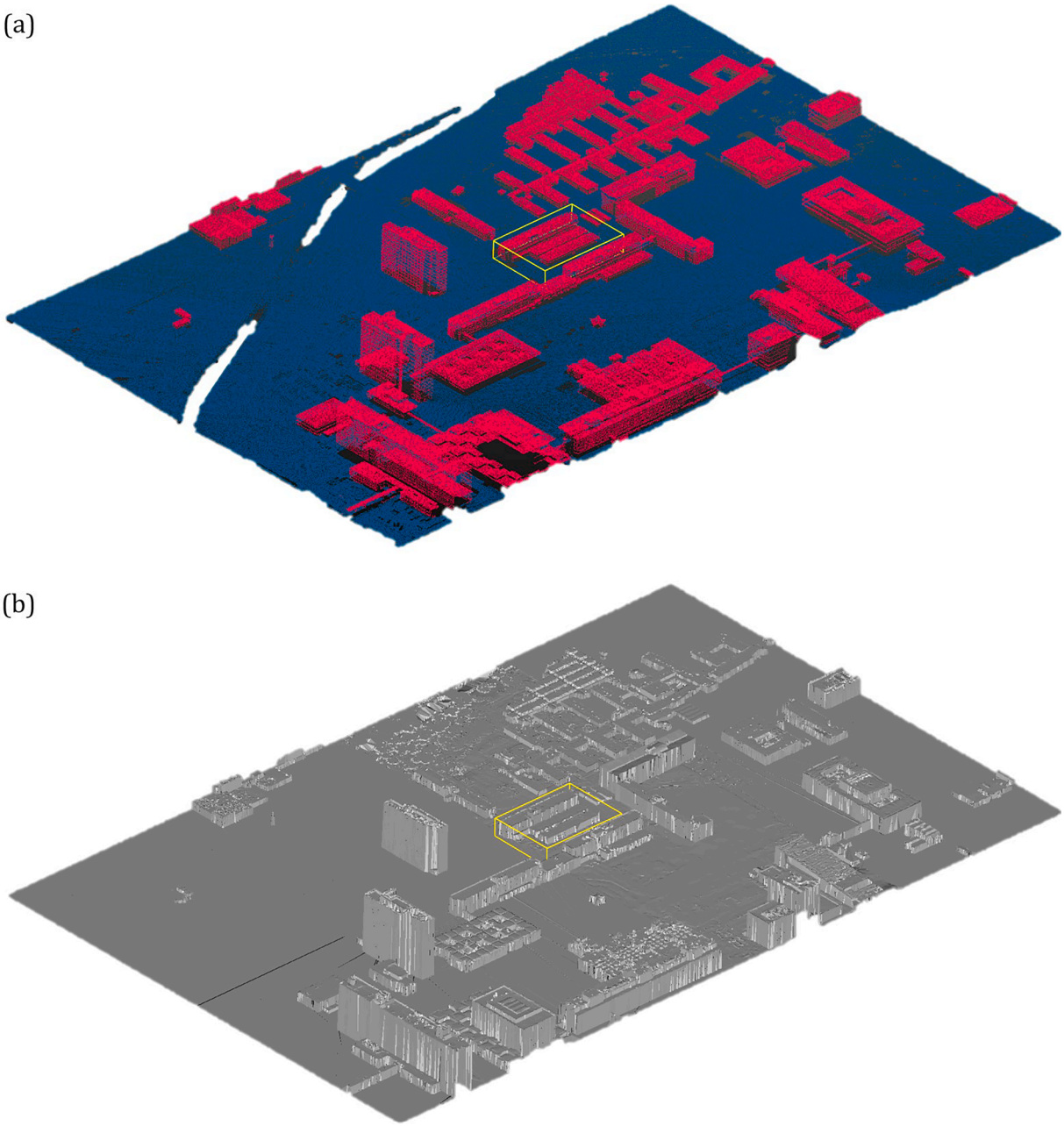


**Fig. 5.** Solid model generation process, with (a) ground and building points from the classified point cloud and (b) reconstructed surface model. The yellow bounding box marks the area for the validation study in Section 3. (For interpretation of the references to color in this figure legend, the reader is referred to the web version of this article.)

Overall, *OA* and *Avg F1* evaluate the global performance of model, while per class F1 score provides insights into the performance on individual classes. This combination enables a thorough understanding of the model's strengths and weaknesses in the segmentation task.

#### 2.1.3. Segmentation performance

The segmentation results on the testing dataset are presented in Table 1, wherein the *OA* and *Avg F1* respectively achieve 94.9% and 93.4%, and the per class F1 scores are also remarkable high. The results indicate that the trained network is able to provide accurate predictions, meeting the requirements of the present work. The segmented point cloud tile (Fig. 4) will be used in the subsequent sections, to demonstrate hybrid model generation procedures and validating the performance of the model in solar irradiance simulation.

### 2.2. Solid model generation

Upon successful segmentation of the testing point cloud tile described in Section 2.1.3, point clouds corresponding to buildings, ground, and trees are processed independently. Employing the solid model reconstruction methodology proposed by Tian et al. [11], a Delaunay triangulation is conducted on the building and ground points to create a solid model suitable for Radiance raytracing DC computations. Fig. 5 provides visualizations of both the input point cloud and the reconstructed solid model.

### 2.3. Fusion model generation

The surfaces generated in Section 2.2 are integrated with the segmented point clouds of trees to generate the fusion model, as shown

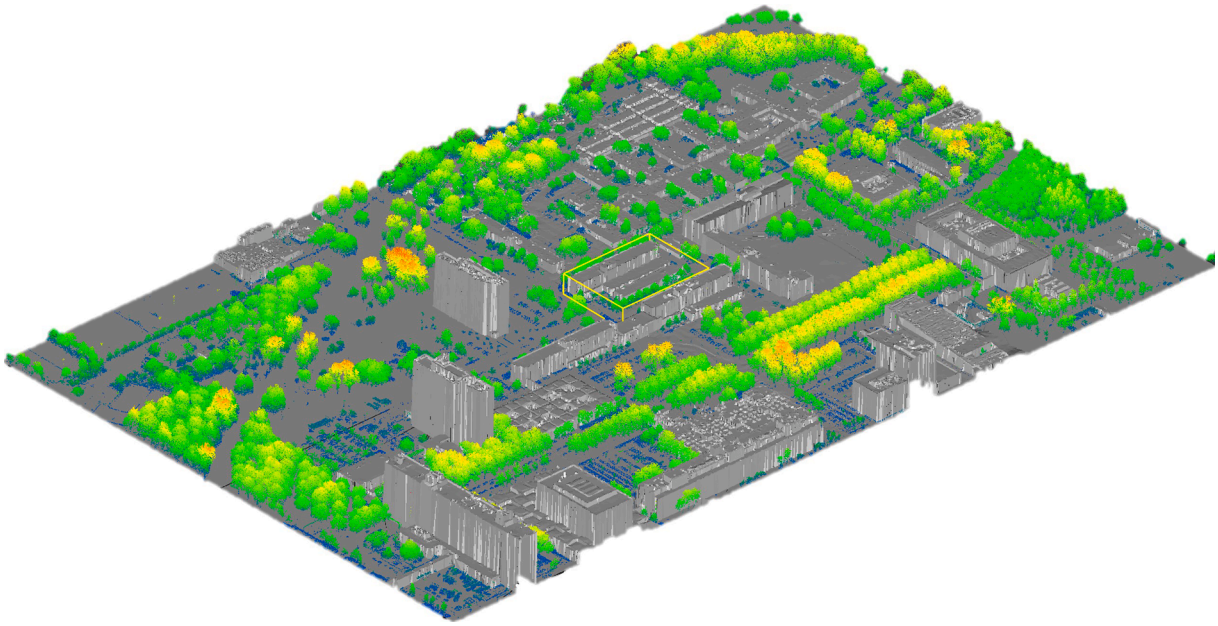

**Fig. 6.** Generated fusion model for subsequent solar irradiance simulation, wherein the yellow bounding box marks the area for the validation study in Section 3. (For interpretation of the references to color in this figure legend, the reader is referred to the web version of this article.)

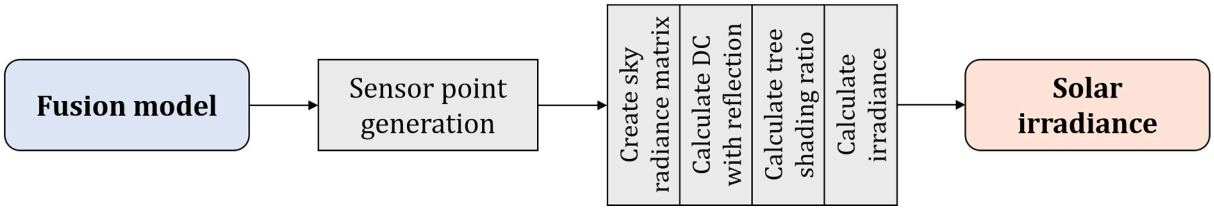


**Fig. 7.** Schematic workflows for modeling solar irradiance from the fusion model.

in Fig. 6. Within the fusion model, the buildings and the ground are represented by well-defined solid models, whereas the trees, in agreement with their irregular morphological characteristics, are present in the form of point clouds.

### 2.4. Solar irradiance modeling

Fig. 7 schematically illustrates the workflow of our proposed fusion model matrix-based solar irradiance modeling method, which consists of sensor point generation and four sequential calculation steps.

#### 2.4.1. Daylight coefficient matrix calculation

Referring to Fig. 7, the first calculation step in the irradiance modeling method is to calculate the *DC* [-] matrix without shading impacts of trees. This step uses the solid elements of the fusion model as input, while the Radiance *rfluxmtx* sub-program is employed to perform raytracing operations to effectively capture the contribution of environmental reflections on *DC* values. Equation (4) illustrates the structure of the calculated *DC* matrix, wherein signs *n, m* represent the number of rows and columns in the discretized sky grid, respectively.

$$DC_{mtx} = \begin{bmatrix} DC_{11} & DC_{12} & \cdots & DC_{1m} \\ DC_{21} & DC_{22} & \cdots & DC_{2m} \\ \vdots & \vdots & \ddots & \vdots \\ DC_{n1} & DC_{n2} & \cdots & DC_{nm} \end{bmatrix} \tag{4}$$

#### 2.4.2. Tree shading ratio matrix calculation

The second calculation step of the present method is using the Pyrano *dc* module to generate a tree shading ratio matrix describing the amount of solar irradiance that is reduced by tree shading impacts. Specifically, the tree shading ratio *TSR* [-] is obtained by Pyrano's cover ratio calculation method (Appendix A.2), and expressed as the ratio of a certain sky segment area is blocked by trees (Equation (5)).

$$TSR_{mtx} = \begin{bmatrix} TSR_{11} & TSR_{12} & \cdots & TSR_{1m} \\ TSR_{21} & TSR_{22} & \cdots & TSR_{2m} \\ \vdots & \vdots & \ddots & \vdots \\ TSR_{n1} & TSR_{n2} & \cdots & TSR_{nm} \end{bmatrix} \tag{5}$$

#### 2.4.3. Sky radiance matrix generation

To calculate the incident irradiance on each sensor point, the sky radiance [W/m$^2$] values of the discretized sky segments should be primarily determined in the form of a sky radiance matrix. Radiance's *gendaymtx* sub-program is called for this task, which uses the global horizontal radiance data as input. The outputs are the solar direct radiance matrix and sky diffuse radiance matrix of each simulation timestep, as shown in Equation (6).

$$G_{mtx\_dir} = \begin{bmatrix} G_{dir\_11} & G_{dir\_12} & \cdots & G_{dir\_1m} \\ G_{dir\_21} & G_{dir\_22} & \cdots & G_{dir\_2m} \\ \vdots & \vdots & \ddots & \vdots \\ G_{dir\_n1} & G_{dir\_n2} & \cdots & G_{dir\_nm} \end{bmatrix}$$
$$G_{mtx\_dif} = \begin{bmatrix} G_{dif\_11} & G_{dif\_12} & \cdots & G_{dif\_1m} \\ G_{dif\_21} & G_{dif\_22} & \cdots & G_{dif\_2m} \\ \vdots & \vdots & \ddots & \vdots \\ G_{dif\_n1} & G_{dif\_n2} & \cdots & G_{dif\_nm} \end{bmatrix} \tag{6}$$

#### 2.4.4. Irradiance modeling

As the last calculation step, by multiplying the *DC* matrix with the

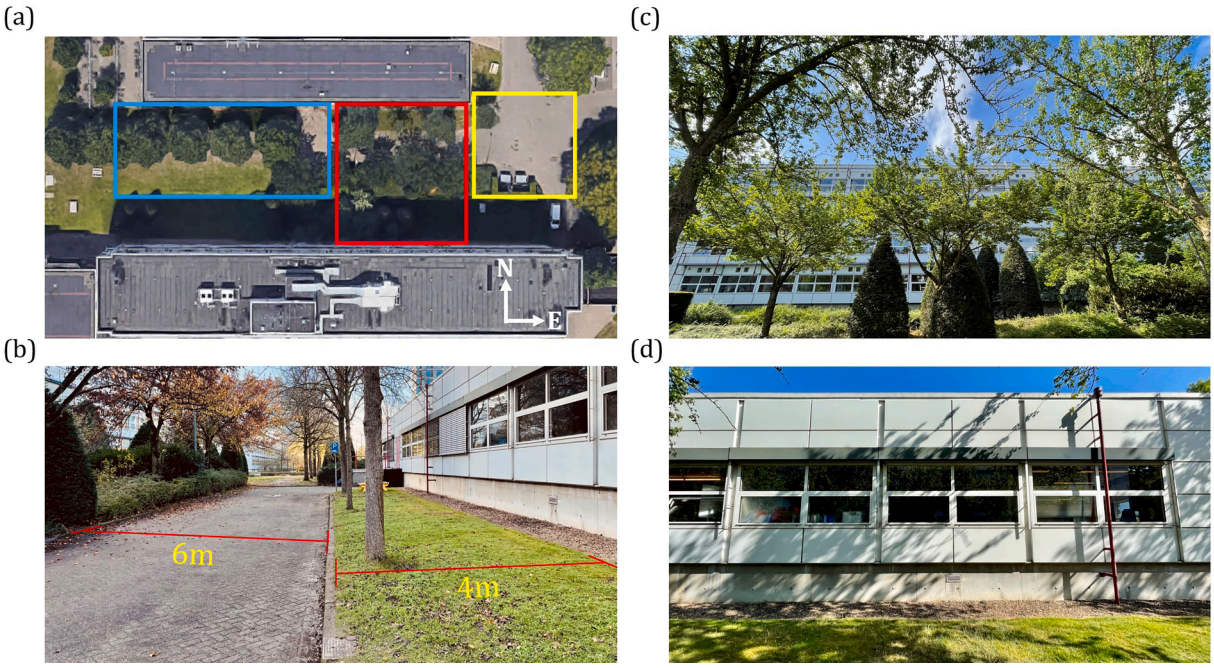


**Fig. 8.** Building canyon in TU/e campus for model validation. (a) Overview of the canyon, where the area for validation and the nearby trees are outlined by the red box, the area is adjacent to an open space (east, yellow box) and several trees (west, blue box); (b) The grassy area and sidewalk in the canyon; (c) Front view of the validation area; (d) Apparent tree shadows on the building façade for validation. (For interpretation of the references to color in this figure legend, the reader is referred to the web version of this article.)

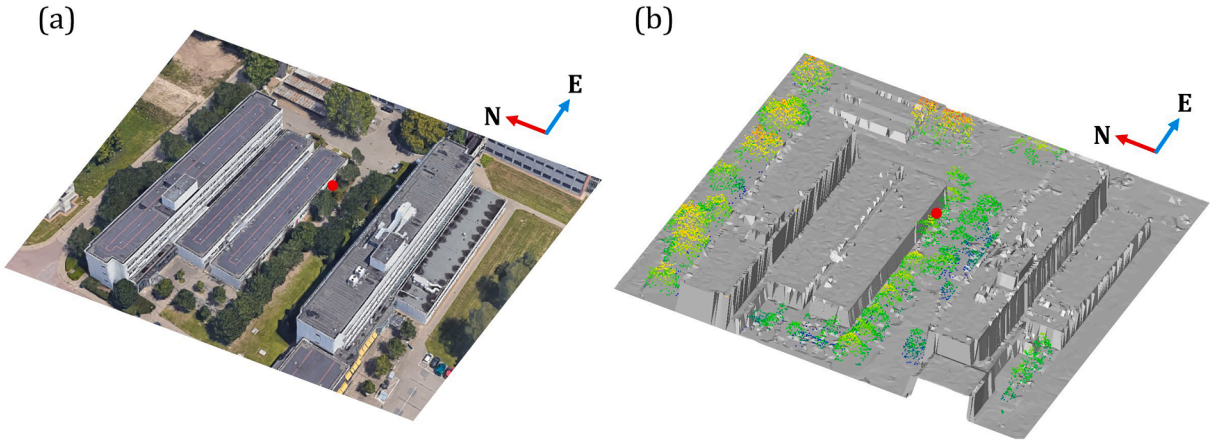


**Fig. 9.** Visualization of the area for irradiance modeling and model validation, the sensor points are highlighted by red dots, with (a) Aerial image and (b) Fusion model. (For interpretation of the references to color in this figure legend, the reader is referred to the web version of this article.)

sky direct radiance matrix and sky diffuse radiance matrix, respectively, the contributions of each sky segment to the direct irradiance [W/m$^2$] and diffuse irradiance [W/m$^2$] without tree shading impacts on the sensor point can be derived, expressed by $E_{mtx\_dir\_without\_tree}$ and $E_{mtx\_dif\_without\_tree}$ in Equation (7)(8) separately.

$$E_{mtx\_dir\_without\_tree} = DC_{mtx} \bullet G_{mtx\_dir} \tag{7}$$

$$E_{mtx\_dif\_without\_tree} = DC_{mtx} \bullet G_{mtx\_dif} \tag{8}$$

After that, by combining $E_{mtx\_dir\_without\_tree}$ and $E_{mtx\_dif\_without\_tree}$ with the tree shading ratio matrix, we calculate the actual irradiance contributions [W/m$^2$] of different sky segments under tree shading impacts, see Equation (9)(10).

$$E_{mtx\_dir} = E_{mtx\_dir\_without\_tree} \bullet (1 - TSR_{mtx}) \tag{9}$$

$$E_{mtx\_dif} = E_{mtx\_dif\_without\_tree} \bullet (1 - TSR_{mtx}) \tag{10}$$

Then, the irradiance components of all sky segments are summed to get the final incident irradiance value on the sensor point. The calculation is shown in Equation (11), where *s, i* are respectively the row and column index of the discretized sky grid.

$$E_{incident} = \sum_{s=1}^{n} \sum_{i=1}^{m} \left( E_{mtx\_dir,s,i} + E_{mtx\_dif,s,i} \right) \tag{11}$$

## 3. Validation study

In this section, we will discuss the model validation process and corresponding results. As mentioned in section 1.3, the fusion model based solar modeling method is validated by both field measurements and inter-model comparison, i.e., the calculated irradiance by the

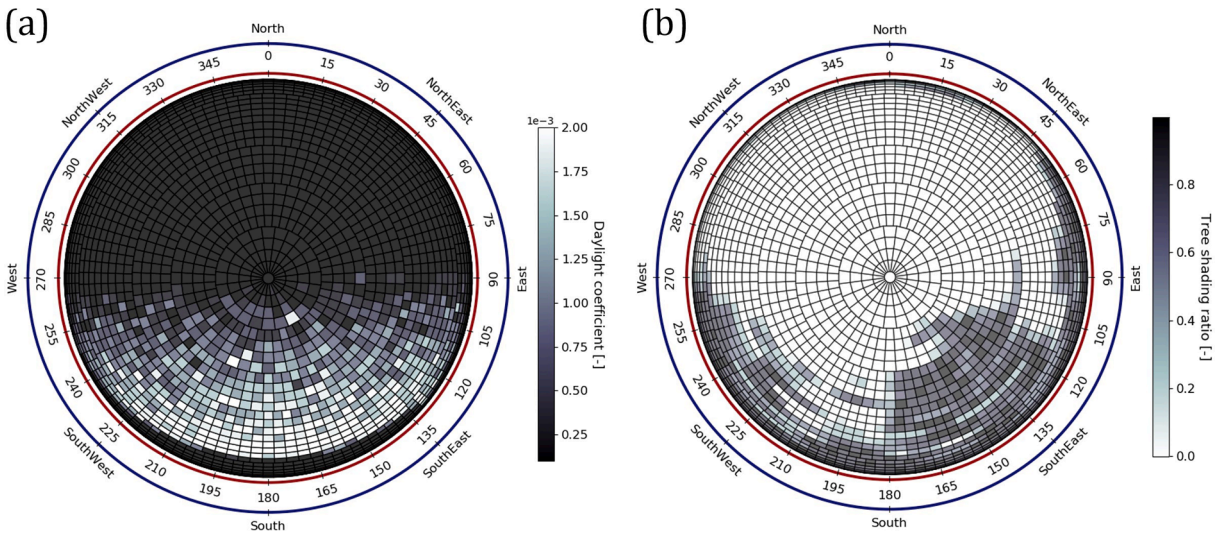


**Fig. 10.** Visualization of (a) simulated DC and (b) tree shading ratio of sky segments.

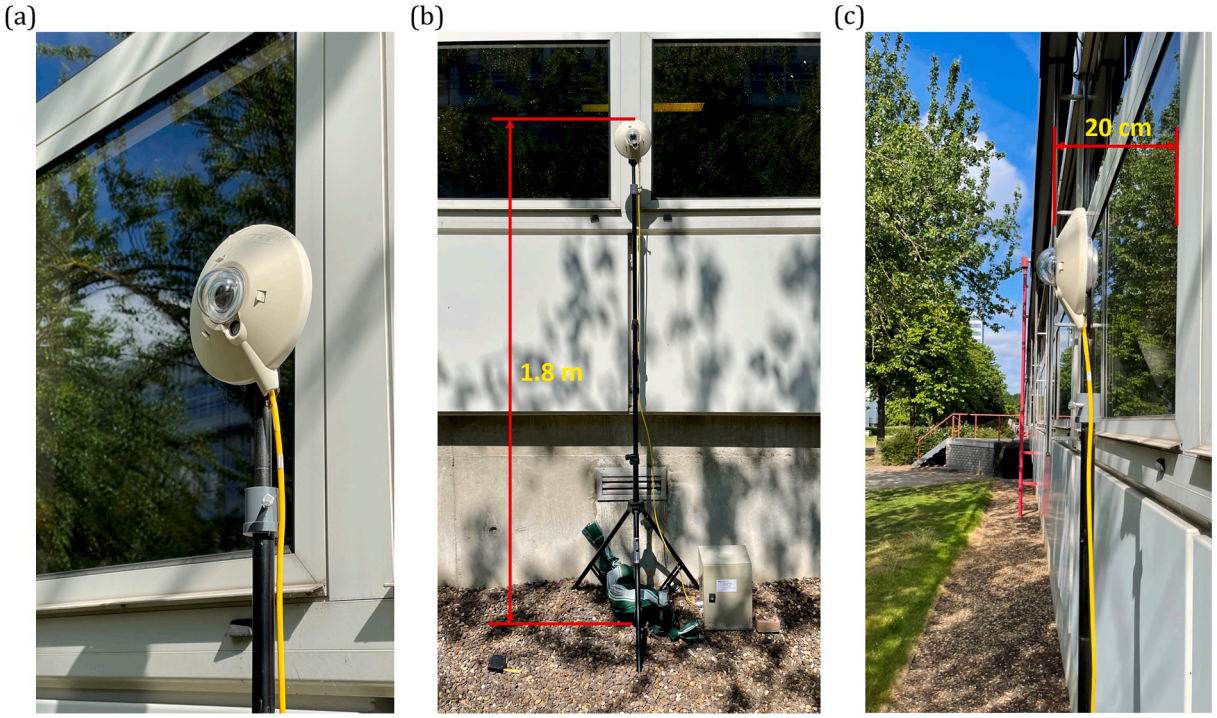


**Fig. 11.** Deployment of the pyranometer for irradiance measurement.

proposed method is compared against field measured data and simulation results obtained with state-of-the-art tree geometric models.

### 3.1. Validation area

The area for model validation is located in an east–west oriented building canyon at the campus of Eindhoven University of Technology (TU/e), the Netherlands (Fig. 8a). At the center of the canyon lies a 6-meter wide sidewalk, bordered by a 4-meter wide grassy area (Fig. 8b), with rows of trees (Quercus robur) planted along its periphery. During daylight hours, the south-facing facades of the buildings are subject to intermittent partial shading caused by the tree canopy (Fig. 8c-d).

In the present study, we positioned the sensor point on the southern façade of the building for both simulation and measurement purposes. This location is anticipated to experience significant partial shading impacts from nearby trees during daylight hours. Fig. 9a and 9b illustrate the sensor point (represented by a red dot) within the validation area, as visualized in an aerial image and the fusion model, respectively.

### 3.2. Irradiance simulation

Following the solar irradiance modeling steps described in Section 2.4, we calculated the incident irradiance in our validation area. To effectively capture the dynamic variation of tree shading impacts, the simulation timestep was set at one minute. The input global horizontal radiance data for simulation was sourced from the SolarBEAT weather station [70] situated on the TU/e campus. Additionally, in the simulation, all the surfaces are assumed as Lambertian diffusers, wherein the building surfaces are assigned a reflectance at 0.3, as recommended by

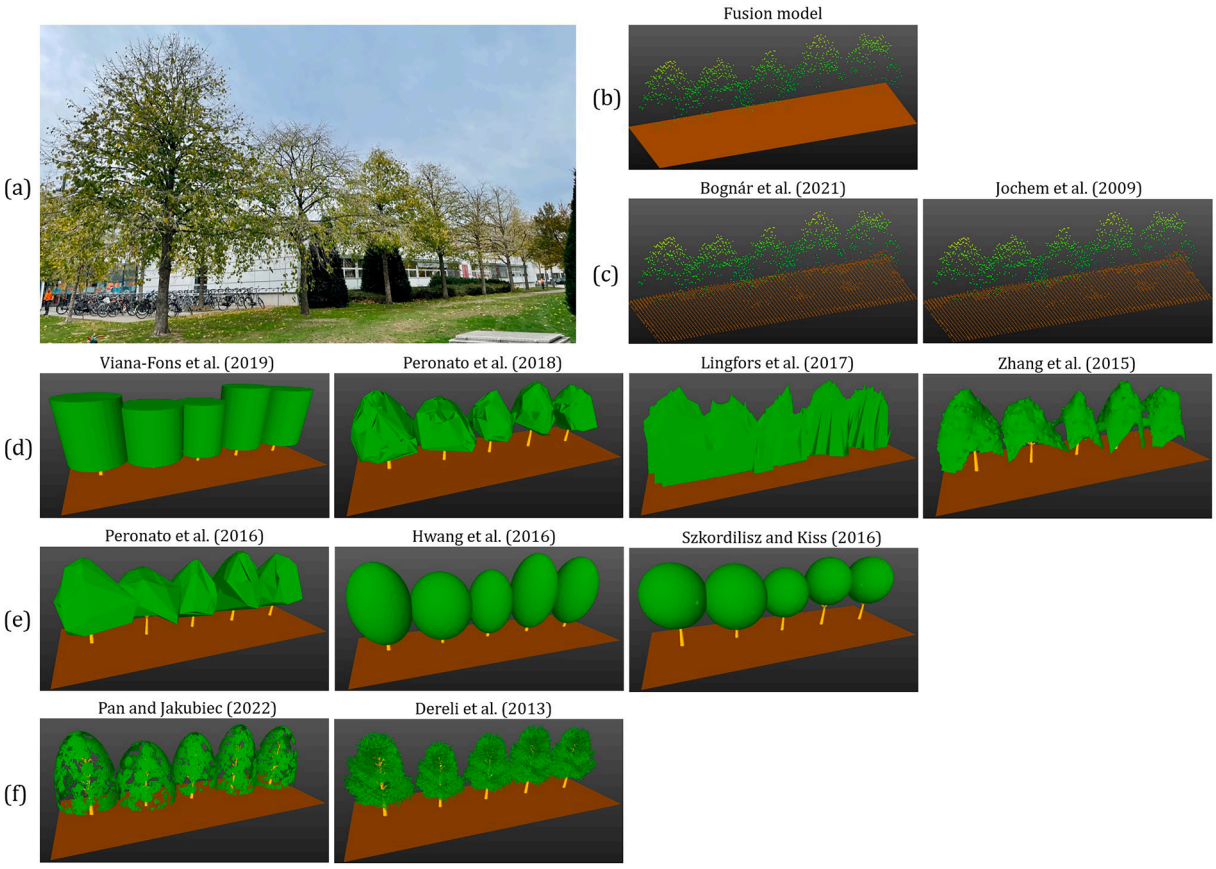


**Fig. 12.** Modeling results of part of the trees in the validation area with representative methods in the state-of-the-art. (a) Actual scene; (b) Trees modeled using proposed hybrid approach; (c) Trees modeled using full point cloud; (d) Trees modeled as opaque solid; (e) Trees modeled as semi-transparent solid; (f) Trees modeled as solid with gaps.

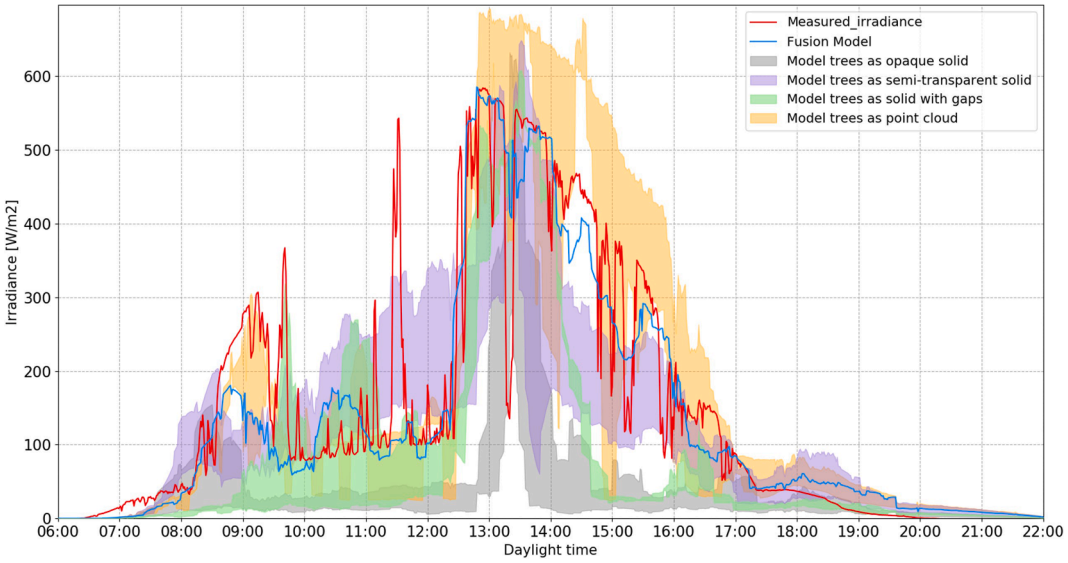


**Fig. 13.** Minute-based irradiance simulation results during daylight time in May 15.

[71]. The ground albedo was set at 0.2, adhering to guidelines from NREL [72], and also confirmed by our experiments. Fig. 10a and 10b visualize the calculated DC matrix and tree shading ratio matrix, respectively, mapped over the discretized sky.

### 3.3. Irradiance measurement

To measure the incoming irradiance at a minute-wise resolution, we deployed a pyranometer in the designated validation area (Fig. 11a), positioned at a height of 1.8 m from the ground and 20 cm away from the façade (Fig. 11b-c). Detailed technical specifications of the

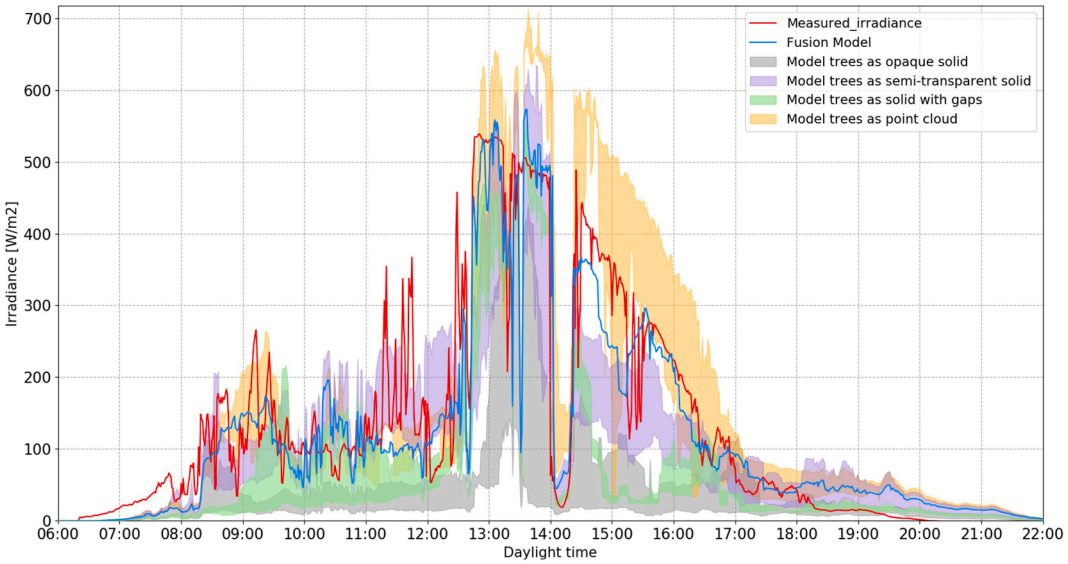


**Fig. 14.** Minute-based irradiance simulation results during daylight time in May 22.

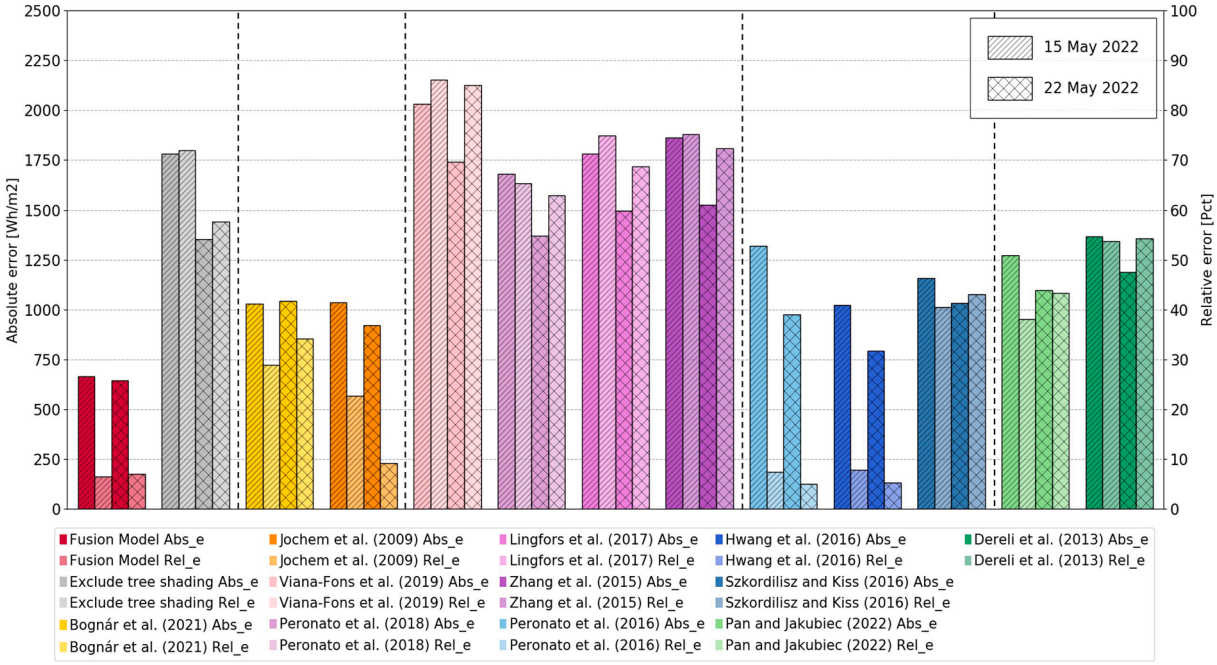


**Fig. 15.** Cumulative error of different models in solar irradiance simulation, with candidate models plotted in different color; Different type of error of the same model of the same model have different color saturation; The results of two days are marked by different hatches.

pyranometer can be found in Appendix B. The data collection period spanned 45 days, commencing on May 10 and concluding on June 23, 2022.

### 3.4. Inter-model comparison

In conducting the inter-model comparison, we examine the results obtained from utilizing eleven different tree geometric models (reviewed in Section 1.1), as inputs for the irradiance simulation. These results are then compared with those derived from our proposed hybrid modeling approach. Fig. 12 illustrates the modeling outcomes for a subset of trees within the validation area, showcasing the differences among the various methods employed.

### 3.5. Results

In this section, we will discuss the results of the validation experiments. The irradiance simulation results, presented at a minute-wise resolution, will be comparatively analyzed in the context of both daily and long-term (45 days) perspectives.

#### 3.5.1. Daily results

Two days featuring predominantly clear skies, May 15 and May 22, were chosen for visualizing and analyzing daily results. Fig. 13 presents the comparison for May 15, where the red line denotes measurement data, the blue line signifies fusion model results, and other colored regions represent the varying ranges of results from different types of tree models. Notably, shading impacts primarily occur between 9:00 and

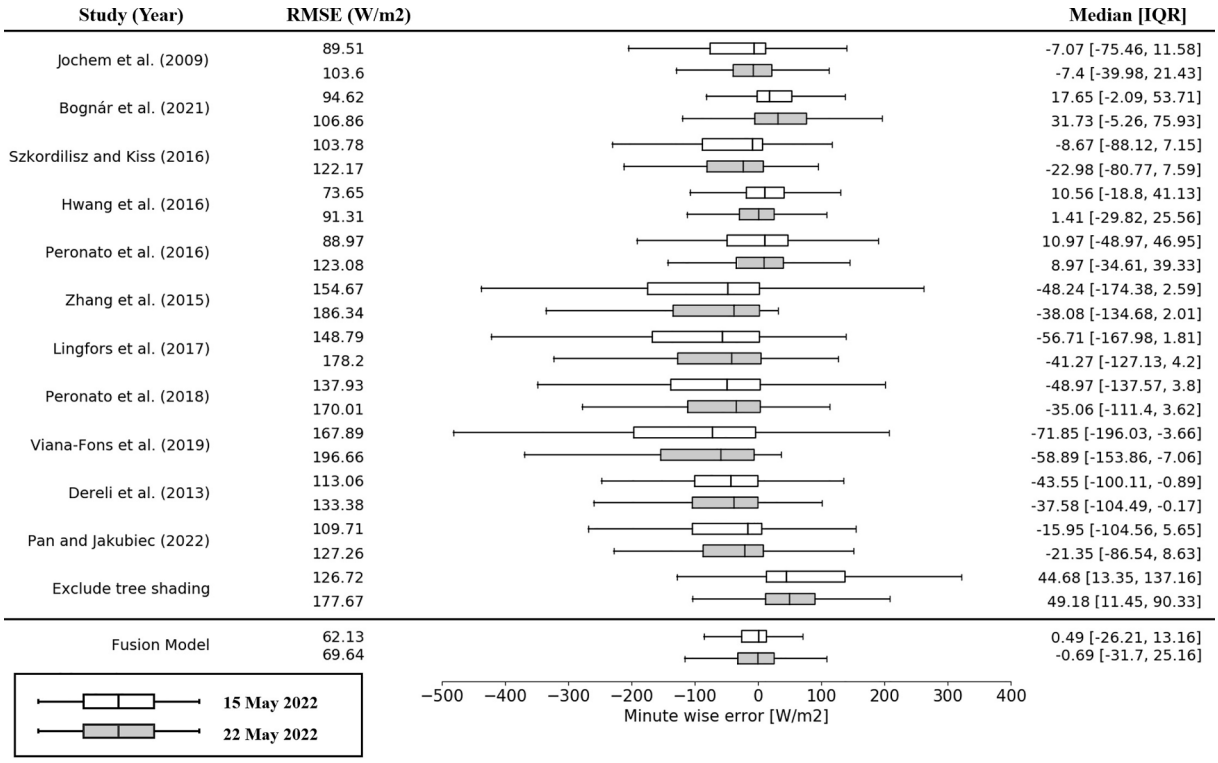


**Fig. 16.** Minute-based error during daylight time of two days, with the results of May 15 in white and May 22 in grey.

12:30, with the fusion model output closely mirroring the measurement data in terms of both trend and value proximity.

Regarding the other type of models, in reference to the measured data, opaque solid models generally underestimate irradiance. Solid models with distributed gaps exhibit performance akin to their opaque counterparts, but their results might oscillate around measured values during peak shading hours in the morning (9:00–12:30). Full point cloud models align well with measurements up to 12:30; however, they significantly overestimate irradiance in subsequent afternoon hours. Semi-transparent solid models overestimate incoming irradiance when apparent shading occurs in the morning, while underestimating incident irradiance during afternoon periods.

The results for May 22, illustrated in Fig. 14, display a similar trend to those of May 15. Both opaque solid models and solid gap models consistently underestimate irradiance values for most timesteps, from morning until 18:00. Full point cloud models performed well in the morning but exhibit marked overestimations after 12:30. In contrast, the fluctuation range of semi-transparent models is lower than the measured data during the afternoon. It is also noteworthy that the measured irradiance surpasses the simulation sets in the morning before 8:00, while falling below the simulation sets after 19:00. These two discrepancies arise from the underestimation and overestimation of albedo reflections in the morning and evening, respectively, which are explored in greater detail in Section 4.1.2.

In order to more intuitively quantify the uncertainty embedded in the simulation results of the different models, we calculate the cumulative irradiation $G_{cumulative}$ [Wh/m$^2$] on the sensor point throughout the daylight time by Equation (12), wherein the $E_{incident,t}$ is the incident irradiance [W/m$^2$] at timestep $t$, and the $T$ is equal to the measurement (simulation) timestep, at 1 min. After that, we can calculate two different metrics for error quantification: the cumulative absolute error *Abs_e* [Wh/m$^2$] (Equation (13)) and the cumulative relative error *Rel_e* [%] (Equation (14)). The *Abs_e* corresponds to the sum of absolute error values from each individual simulation timestep throughout the day. This metric serves to illustrate how well the minute-based simulation outcomes align with measurements, accentuating the discrepancies in model robustness in the context of dynamic tree shading scenarios. In contrast, *Rel_e* stands for the ratio of the aggregated error from all timesteps relative to the measured $G_{cumulative}$. This ratio reflects the model's precision against daily-based energy harvesting simulation results, thereby providing an enhanced evaluation of the model's overall performance.

$$G_{cumulative} = \sum_{t=1}^{k} E_{incident,t} \bullet T \tag{12}$$

$$Abs\_e = \sum_{t=1}^{k} \left| E_{incident\_simulated,t} - E_{incident\_measured,t} \right| \bullet T \tag{13}$$

$$Rel\_e = \frac{\left| \sum_{t=1}^{k} \left( E_{incident\_simulated,t} - E_{incident\_measured,t} \right) \bullet T \right|}{G_{cumulative\_measured}} \times 100\% \tag{14}$$

Fig. 15 illustrates the cumulative error for various models across the two evaluation days, with the primary axis representing the *Abs_e* and the secondary axis indicating the *Rel_e*. The fusion model shows the lowest absolute error (approximately 650 Wh/m$^2$) and predominantly lower relative error (approximately 7%) for both days. These results suggest that the fusion model delivers superior performance in terms of accurately modeling irradiance across most timesteps in the context of tree shading. Additionally, it demonstrates a significant reduction in errors inherent in daily-based solar irradiation modeling. This performance is followed by the approaches of Peronato et al. (2016) and Hwang et al. (2014), which model trees as semi-transparent solids with relative errors ranging from 5% to 8%; nonetheless, the absolute errors observed in the model by Peronato et al. (2016) were approximately 250 Wh/m$^2$ greater than those of Hwang et al. (2014) on both days, underscoring the disparity in accuracy between the two models when applied to minute-based irradiance modeling.

Regarding the full point cloud models, their cumulative absolute errors remain at a level comparable to the semi-transparent models, but their corresponding relative errors are markedly higher. The two

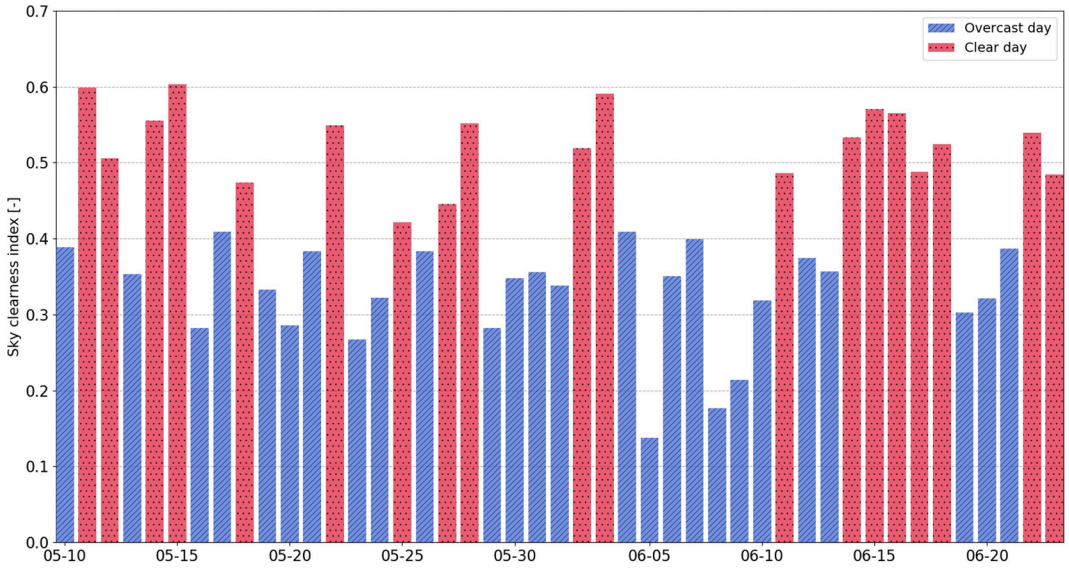


**Fig. 17.** Calculated sky clearness index during the validation period, wherein days with clear sky are in red, days with overcast sky are in blue. (For interpretation of the references to color in this figure legend, the reader is referred to the web version of this article.)

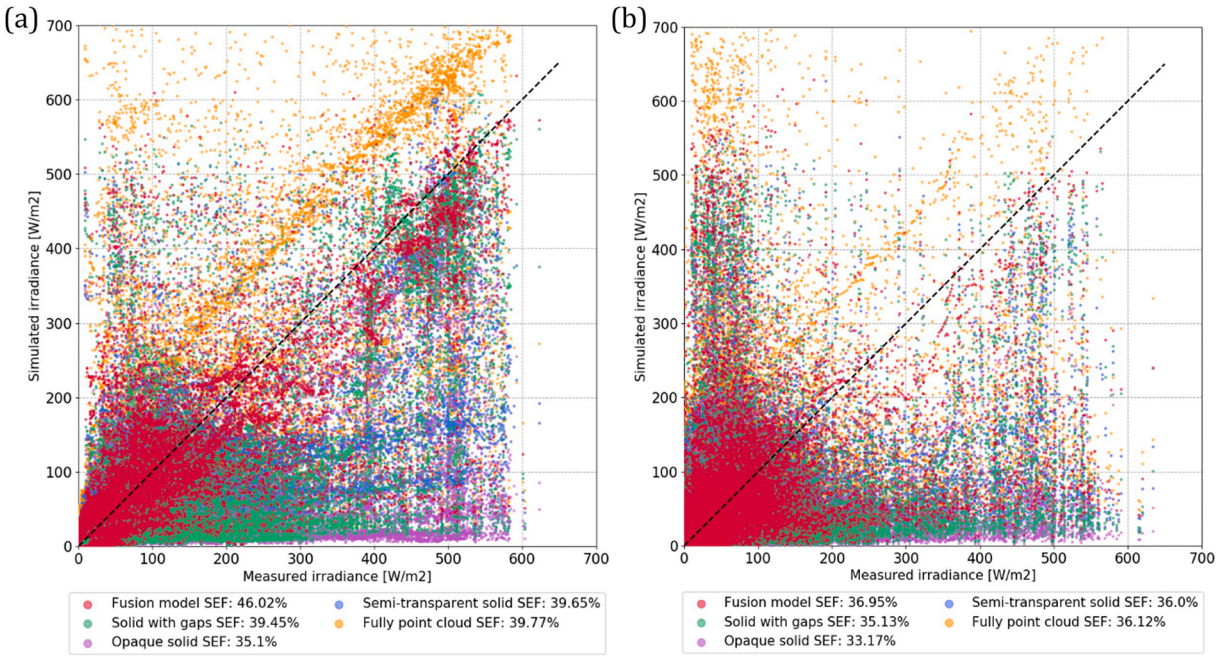


**Fig. 18.** Results of simulations during the whole validation study with different models, with (a) days with mostly clear sky and (b) days with mostly overcast sky.

methods that model trees as solids with gaps yield nearly identical absolute error values (approximately 1350 Wh/m$^2$ on May 15 and 1150 Wh/m$^2$ on May 22). However, the relative error of Dereli et al. (2013) at 55% is noticeably higher than that of Pan and Jakubiec (2022), which is around 40%. Finally, for the opaque solid models, both the absolute and relative errors are substantially higher compared to the other models, demonstrates their relatively worse performances in both modeling minute-based irradiance and estimating daily cumulative irradiation. The most poorly performing model exhibits relative errors of roughly 85%, exceeding the error observed in the case where trees are excluded from the simulation.

To further examine the minute-wise error distribution throughout the day, we generated box plots (Fig. 16) and computed the daily Root Mean Squared Error (*RMSE*) [W/m2] using Equation (15). In Fig. 16, the results from various models are displayed in separate rows, with the final row representing the fusion model proposed in this study. Additionally, to aid data analysis, the last column provides the median of the minute-based errors recorded throughout the day, alongside the corresponding interquartile range (IQR). It is evident that the fusion model exhibits the remarkable smallest interquartile range and data dispersion among all cases. Additionally, the *RMSE* of the fusion model is significantly lower than that of other models on both days.

In terms of the median value of the daily error, the fusion model's medians are closest to zero (0.49 W/m$^2$ and −0.69 W/m$^2$ for the two days), whereas other models show medians that are either considerably larger or smaller than zero. This observation suggests that the fusion model can provide more reliable irradiance simulation results with fewer embodied errors for a daily scope. The high temporal resolution data (short timesteps) provided by the fusion model can ultimately enhance PV module performance prediction, facilitating a more

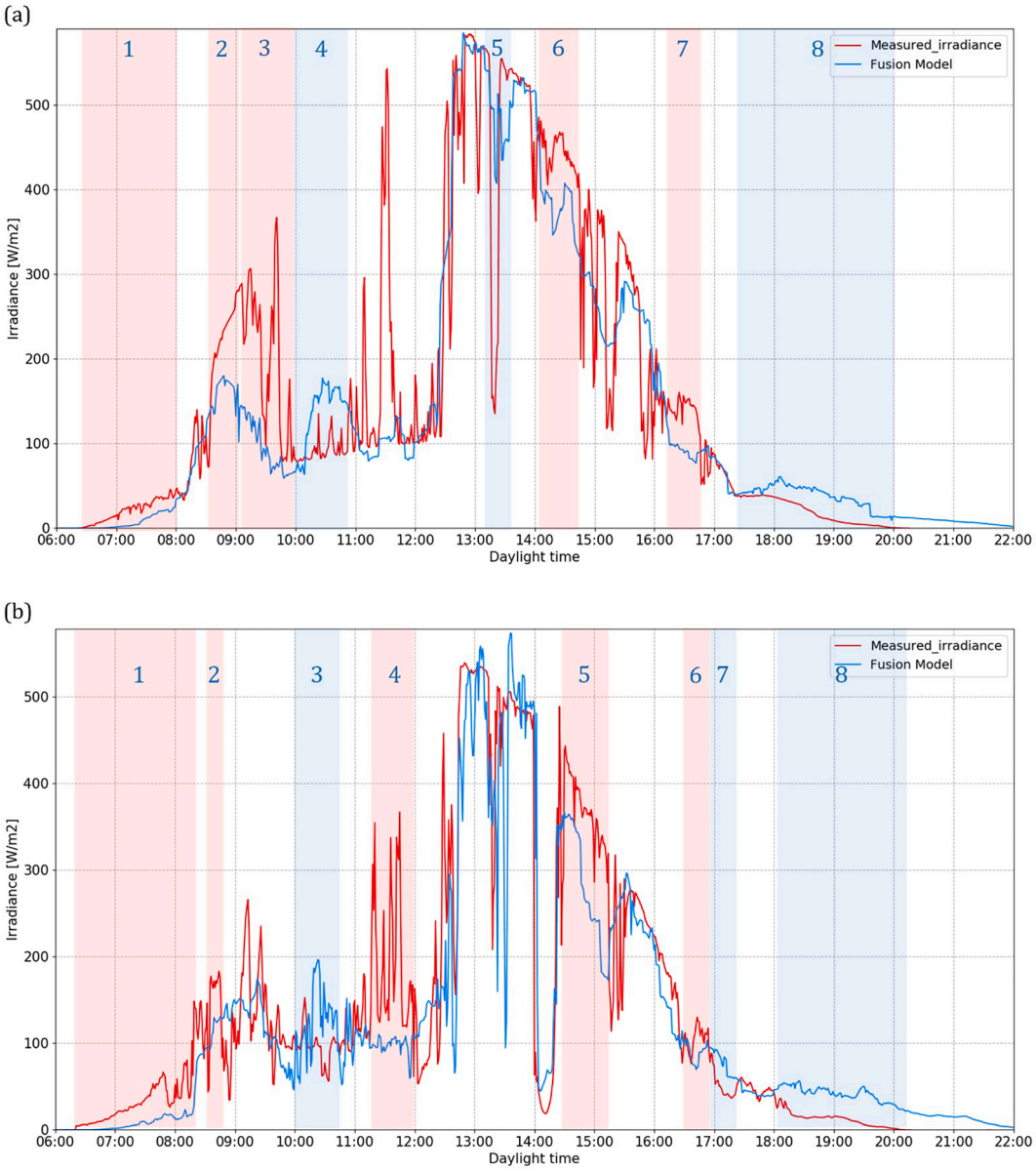


**Fig. 19.** Major irradiance discrepancies in the two days for analysis, with (a) May 15 and (b) May 22.

accurate quantification of mismatch losses under dynamic tree shading impacts. In addition, from Fig. 16 we can also observe that Peronato et al. (2016) and Hwang et al. (2014) also have medians closer to 0. Analogous to the fusion model, they exhibit a more uniform data dispersion on either side of the box plot, as evidenced by the similar absolute values of the first and third quartiles. This characteristic effectively accounts for their smaller cumulative relative errors in Fig. 15, as the errors arising from overestimation and underestimation tend to counteract each other.

$$RMSE = \sqrt{\frac{1}{k} \bullet \sum_{t=1}^{k} \left(E_{simulated,t} - E_{measured,t}\right)} \tag{15}$$

### 3.5.2. Long-term results

To evaluate the performance of different models in solar irradiance simulation for a longer-term period, we performed a thorough data analysis comparing the measured data and the simulation results over the entire measurement period (45 days). The results are examined according to different sky conditions, i.e., clear sky and overcast sky, as characterized by the sky clearness index $K_T$ [-] [73]. Equation (16) illustrates the calculation of sky clearness index, which is defined as the ratio of global horizontal irradiation (*GHI*) against extraterrestrial solar irradiation. The daily sky clearness index during the measurement period as shown in Fig. 17, using $K_T = 0.42$ as a threshold to distinguish days with generally clear and cloudy skies.

$$K_T = \frac{1}{k} \bullet \sum_{t=1}^{k} \frac{GHI_t}{G_{extraterrestrial,t}} \tag{16}$$

To facilitate a more comprehensive analysis among different sets of simulation results, we introduce an additional performance metric, referred to as the small error fraction (*SEF*) [%]. The *SEF* is quantified as the proportion of simulated data points with relative error of less than 20% compared to the corresponding actual data (Equation (17)).

$$SEF = \frac{N_{relativeerror<20\%}}{N_{total}} \times 100\% \tag{17}$$

Fig. 18a and 18b present scatter plots illustrating the long-term simulation results under clear sky and overcast sky conditions,

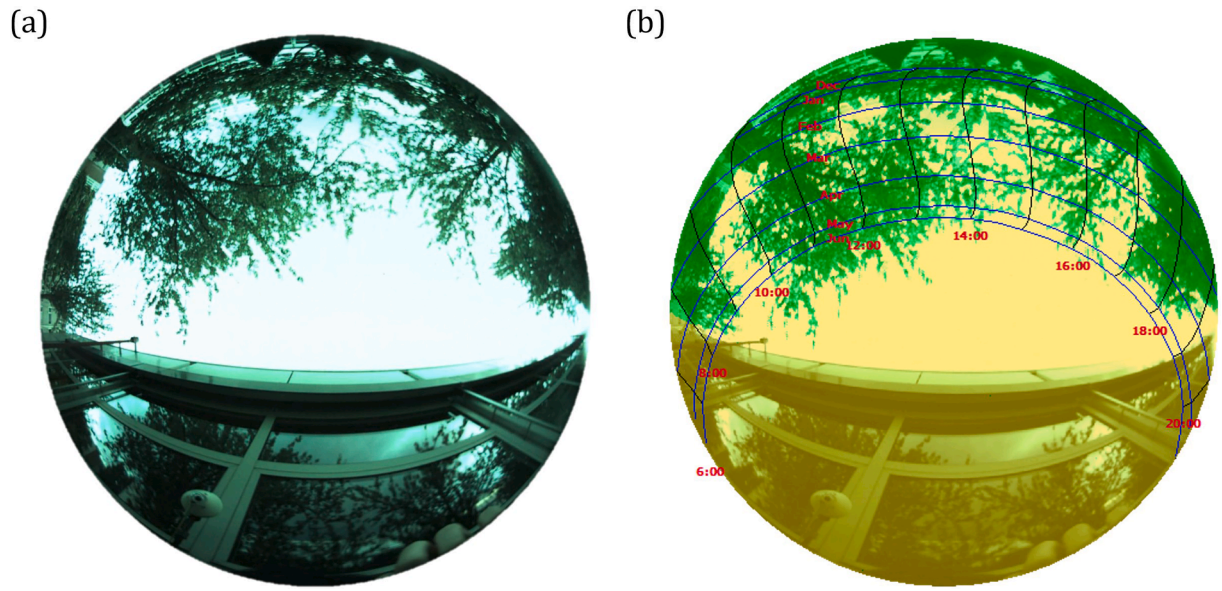


**Fig. 20.** Fisheye photo captured by SunEye-210 for data analysis, with (a) original photo and (b) processed photo with highlighted obstructions (in green) and solar path. (For interpretation of the references to color in this figure legend, the reader is referred to the web version of this article.)

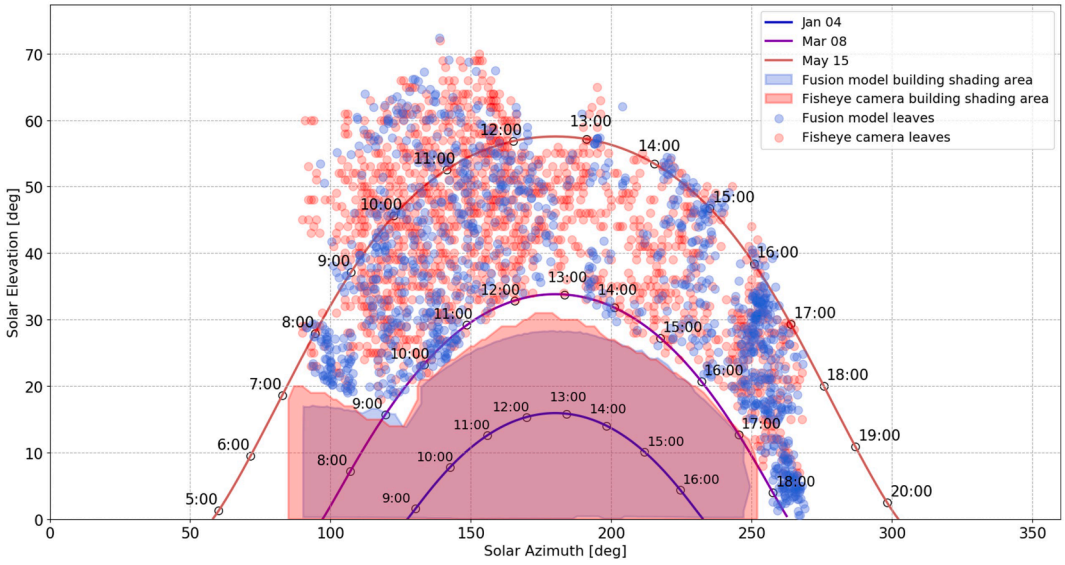


**Fig. 21.** The resampled solar obstructions from fisheye photo (in red) and fusion model (in blue) in the orthogonal solar azimuth-elevation coordinate. (For interpretation of the references to color in this figure legend, the reader is referred to the web version of this article.)

respectively. In each subplot, the x-axis represents the measured data, while the y-axis corresponds to the simulated irradiance. For clear sky results, the fusion model demonstrates remarkable performance, with the majority of data points distributed along the diagonal line. The *SEF* of the fusion model also exhibits the highest value at 46.0%, significantly surpassing other models, which aligns with our findings in Section 3.5.1 that the fusion model provides more accurate results under dynamic partial shading conditions induced by trees.

Regarding the results of other models under clear sky, the solid models with gaps and semi-transparent models show similar performance, with a portion of their simulated data points closely aligned with the measured values during high-irradiation periods (>400 W/m$^2$); however, the irradiance results are predominantly underestimated for the remaining timesteps. Modeling trees as opaque solids results in a substantial underestimation of irradiance values for numerous timesteps, with most data points situated at the bottom of the chart. Moreover, scatter points of full point cloud models also show a trend of distribution along the diagonal, but generally overestimate irradiance data with *SEF* at 39.8%. The overestimation in point cloud models arises from assuming uniform sky segment contributions to reflections, as discussed in Section 1.2.2. For the complex urban scene considered in this study, the reflection contribution varies considerably across the sky segments, leading to inevitable errors when assuming equivalent contributions.

As for overcast sky results, the fusion model does not significantly outperform other models as in the case for clear sky; nevertheless, it still exhibits the highest *SEF* at 36.95%. A higher concentration of the fusion model's data points is observed near the diagonal, particularly for irradiation conditions with measured irradiance ranging from 200 W/m$^2$ to 550 W/m$^2$. For the full point cloud models, as with clear sky results, irradiance is consistently overestimated during most timesteps, yielding a *SEF* of 36.12%. Moreover, the performance of gapped-solid

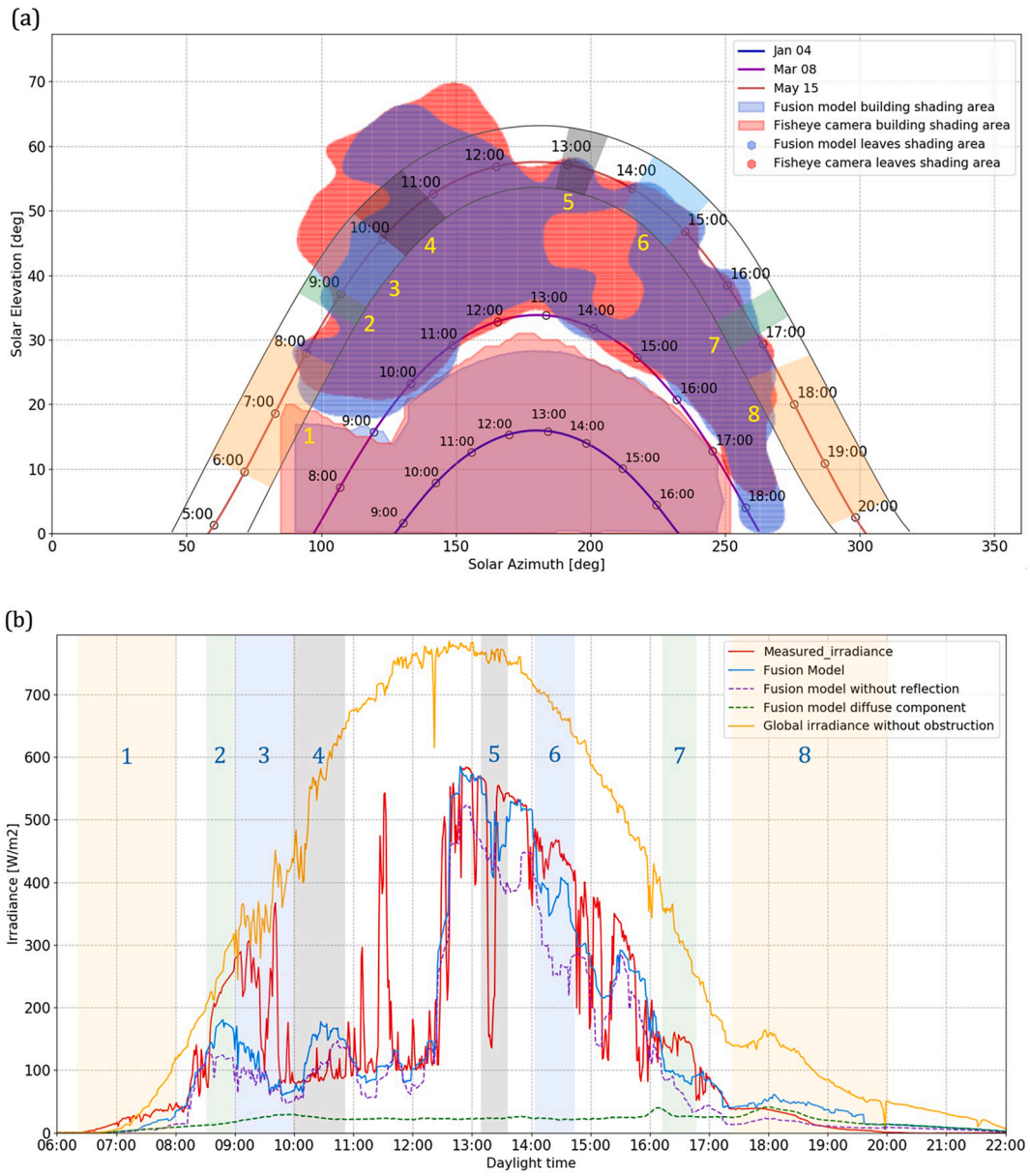


**Fig. 22.** Marked major discrepancies between fusion model output and measured data on May 15 with (a) tree shading area SVM prediction results and (b) minute-based irradiance data. The discrepancies with different causes are highlighted by different colors.

and semi-transparent models remains relatively consistent, with significantly overestimated and underestimated data points evenly distributed in areas close to the axes. Finally, opaque solid models continue to exhibit the poorest performance, with a considerable number of underestimated data points discernible along the x-axis.

## 4. Discussion

The purpose of the present study is to develop and validate a hybrid point-cloud and surface model based method for solar irradiation modeling under partial shading impacts of trees. Through validation experiments, we demonstrate the outstanding performance of the hybrid model. In the following subsections, we will analyze the primary sources of error in the simulations, and provide a comprehensive discussion on the significance, limitations and outlook of the present study.

### 4.1. Presence of discrepancies

In the inter-model comparison, the fusion model outperformed state-of-the-art models. However, as shown in Figs. 13 and 14, there are still notable discrepancies between the results of the fusion model and the actual measurements at some specific timesteps. In this section, we will delve into the potential causes behind these observed discrepancies.

#### 4.1.1. Identification of major discrepancies

To visualize the discrepancies between fusion model outputs and the measured data more intuitively, we have plotted these two sets of data separately in Fig. 19, where the periods with significant discrepancies are highlighted by colors with serial numbers. Periods of major underestimation are marked in red, while overestimations are indicated in blue. For the results of May 15 (Fig. 19a), it can be found that the irradiance was underestimated during five time periods, including early morning, while overestimated in three periods, one of which occurred in the evening. For May 22 (Fig. 19b), we found a similar underestimation

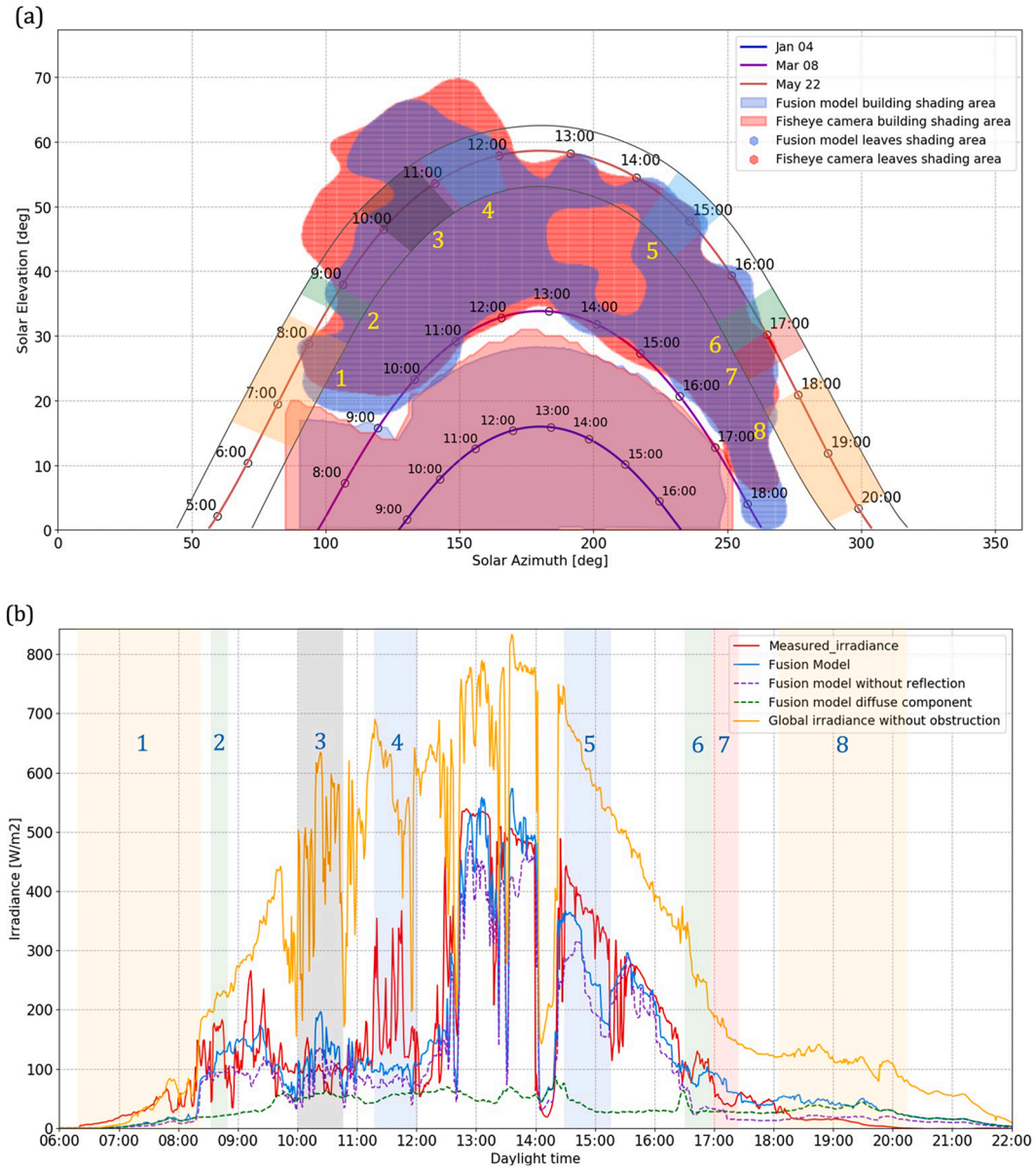


**Fig. 23.** Marked major discrepancies between fusion model output and measured data in May 22 with (a) tree shading area SVM prediction results and (b) minute-based irradiance data. The discrepancies caused by different reason are highlighted by different colors.

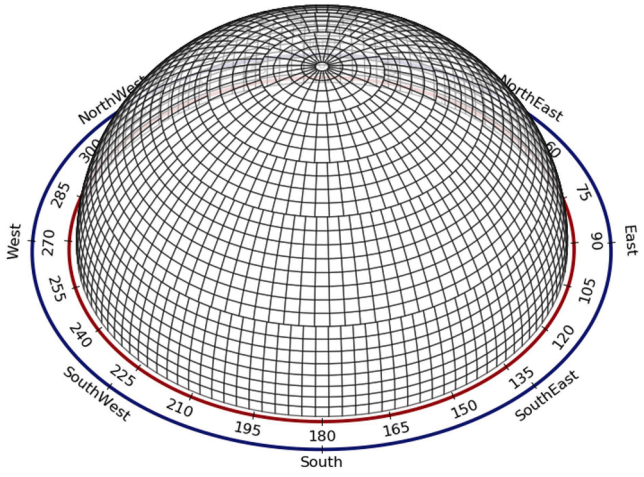


**Fig. A1.** Generated discretized sky with 2305 sky segments.

and overestimation pattern in morning and evening time.

#### 4.1.2. *Reasons for discrepancies*

To investigate the reasons for the major discrepancies in irradiance data under shading impacts, a horizontal fisheye photo of the validation area was captured by a SunEye-210 portable shade evaluation camera, manufactured by Solmetric. SunEye-210 has a built-in GPS and solar shading assessment system, which is able to process the original captured photo (Fig. 20a) to the photo with highlighted shading obstructions and annual local solar path throughout the sky (Fig. 20b).

The obstructions identified in the fisheye photo were classified into two categories: building obstructions and leaf obstructions. Both types of obstructions were subsequently resampled and projected onto an orthogonal solar-azimuth elevation chart, as illustrated in Fig. 21. In this figure, red dots denote resampled leaf points, while red solid areas correspond to the resampled buildings. The coordinate positions of these fisheye photo-resampled obstructions align with their respective locations in the solar path depicted in Fig. 20b.

Obstructions derived from the fusion model, which includes point

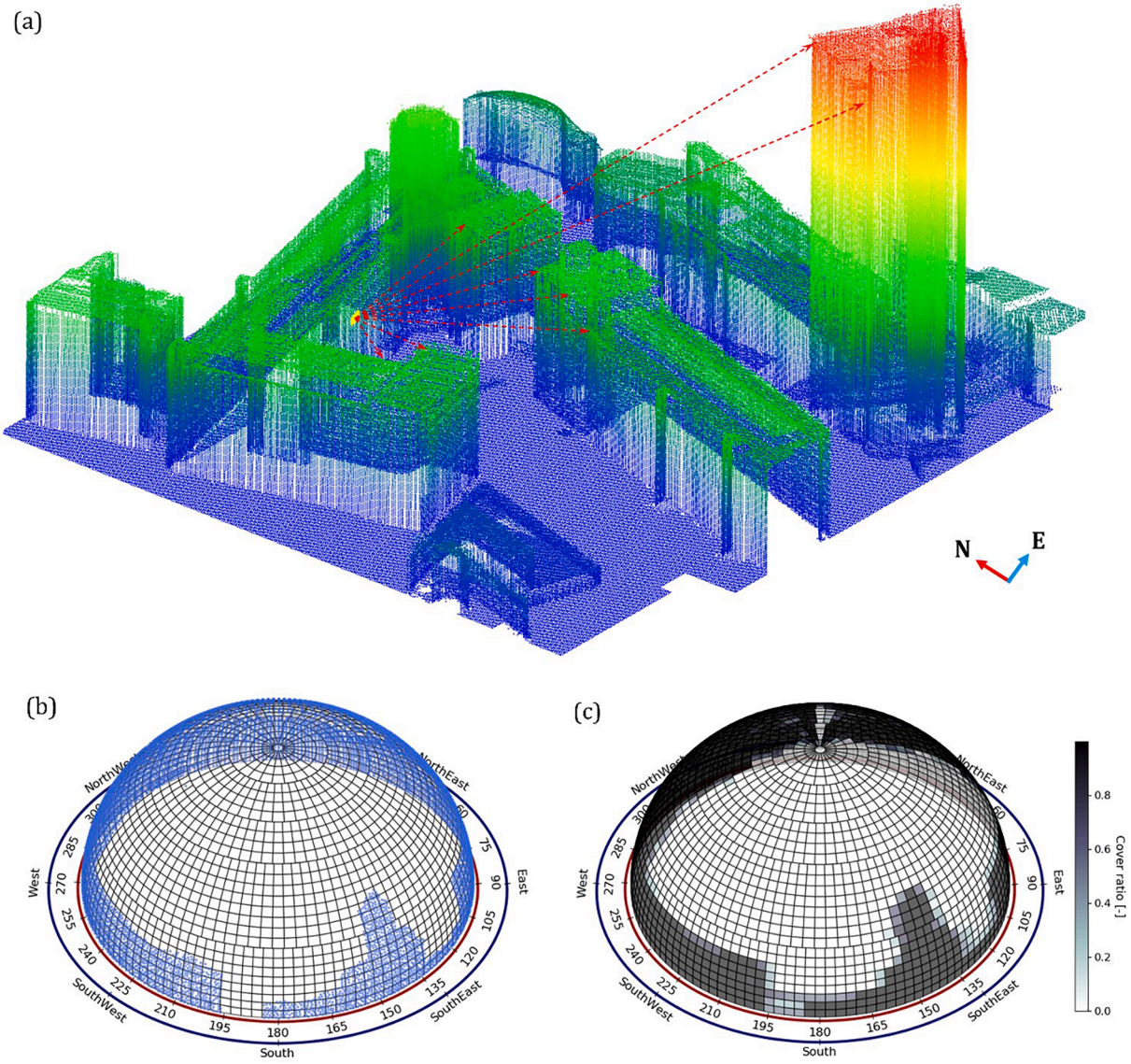


**Fig. A2.** Example of Pyrano sky segment cover ratio calculation: (a) Point cloud (in color ramp) and sensor points (highlighted by yellow) for calculation; (b) Projected point cloud on the discretized sky hemisphere; (c) Calculated cover ratio from point projection results. (For interpretation of the references to color in this figure legend, the reader is referred to the web version of this article.)

clouds of trees and solid models of buildings, were also resampled and displayed in a manner consistent with the information in the fisheye photo (Fig. 21). Furthermore, to demonstrate the workflow, the solar paths for the analysis day (May 15) and two additional days in January and March, characterized by varying solar paths, were plotted on the chart. It is worth noting that the building block dimensions in the fusion model are smaller than those in the fisheye photo. This observation aligns with the findings of Tian et al. [11], who reported that building solid models experience shrinkage during the reconstruction process.

In Fig. 21, it is observed that the solar path on May 15 does not directly intersect the building; instead, it traverses the region with leaf points. Consequently, it can be inferred that the primary source of direct shading in the area under investigation stems from the leaves and branches. Nevertheless, the substantial overlap between the leaf points from both datasets, coupled with the pronounced disparities in point density, complicates the specific analysis and comparison of the time and locations where shading impacts manifest. To tackle this challenge, we utilized Support Vector Machine (SVM) classifications [74] to delineate the leaf areas in the distinct models, thereby determining the sky regions blocked by leaves in both the fusion model and fisheye photo. By scrutinizing the variations in the predicted leaf areas across the two models, we can more precisely pinpoint the factors that give rise to the major discrepancies between the simulation outcomes and the measured data. A comprehensive explanation of the SVM-based leaf shading area determination methodology is presented in Appendix C.

The determined leaf area for May 15 is illustrated in Fig. 22a, where the red region denotes the actual leaf shading area derived from fisheye photo, while the blue region represents the shading area within the fusion model. The solar paths for periods associated with significant discrepancies in Fig. 22a are marked by colored blocks, with respective serial numbers that correspond to the serial numbers of the discrepancies in the irradiance comparison results in Fig. 22b. To further streamline the analysis, we simulated the irradiance considering two more scenarios: one without reflections and disregarding all obstructions, and another accounting for the diffuse component within the incident irradiance at the sensor point. The simulation results of non-reflection case and diffuse component are presented in Fig. 22b alongside the previously mentioned fusion model results and the measured data.

In Fig. 22a, the solar path shows minimal obstruction until 8:00 am

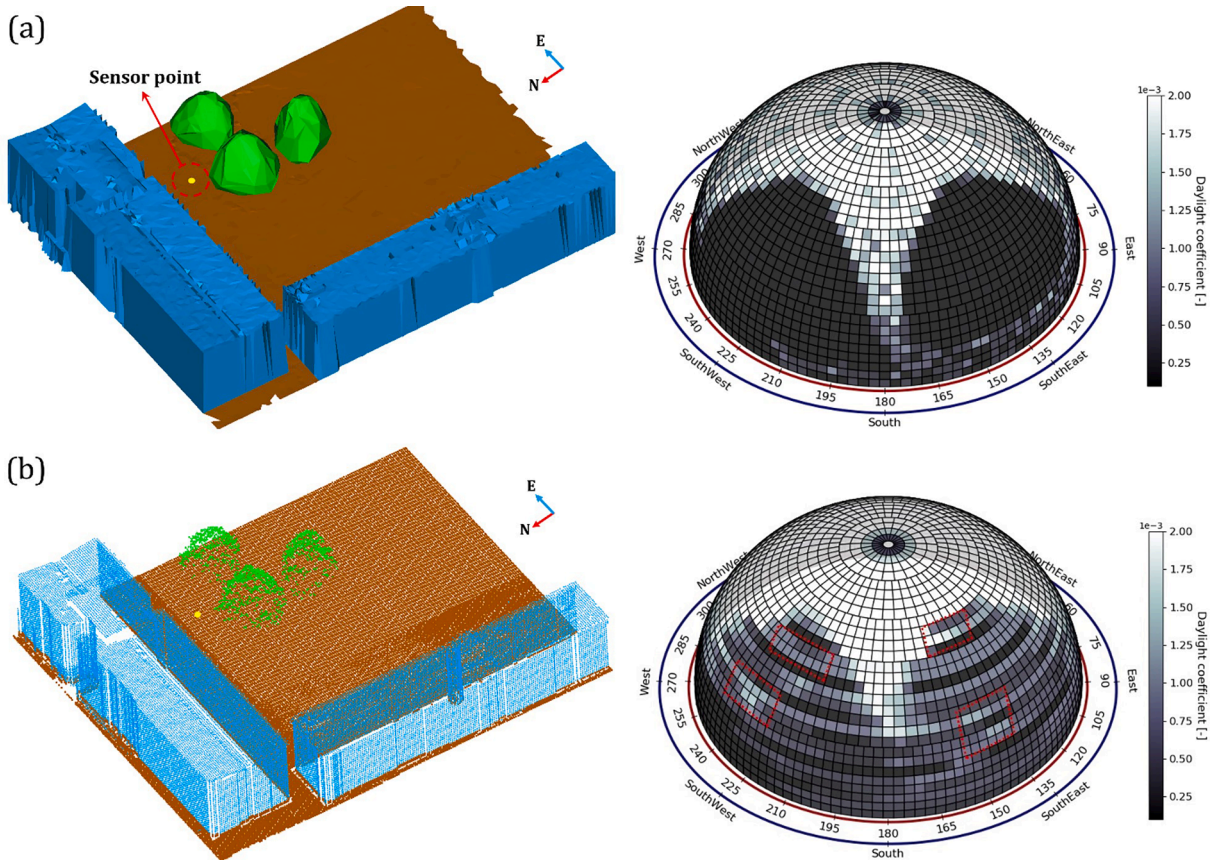


**Fig. A3.** Estimated daylight coefficient distribution over the discretized sky hemisphere with (a) Radiance matrix-based method and (b) Pyrano matrix-based method.

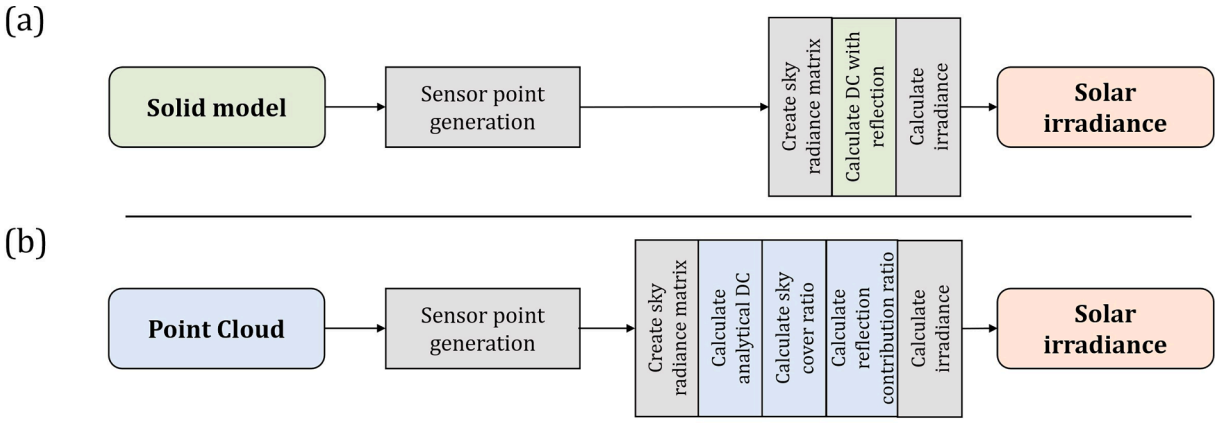


**Fig. A4.** Schematic workflows for simulating solar irradiance with (a) Radiance matrix-based method, (b) Pyrano matrix-based method.

(Index 1) on May 15 and between 17:30 and 20:00 (Index 8). Despite this, the modeled incident irradiance of the fusion model in Fig. 22b reveals clear discrepancies when compared to the measured values during these time intervals.

In the morning hours (Index 1), the fusion model results, both considering and excluding reflections, show minor differences and are consistently below the measured values, indicating a less substantial reflection component. Fig. 22b further highlights the diffuse component as a marginal contributor to the total incident irradiance in these morning hours. Analyzing these findings with the visual context of Fig. 8a, it can be inferred that the morning discrepancy is primarily due to the underestimated direct irradiance component reflected from the eastern open space. Despite trees obstructing a large portion of the sky diffuse irradiance, the minor role of diffuse component at this time suggests the underestimated albedo reflection from eastern side likely drives the observed morning discrepancy.

In contrast, during evening hours (Index 8), the fusion model's outputs diverge, with the results incorporating reflections exceeding the measured values, while those excluding reflections remain lower. This divergence underscores an increased reflection component in the evening compared to the morning hours, indicating an overestimation of albedo reflections from the western, tree-covered area. As the diffuse component dominates the incident irradiance during these hours, this overestimated reflection significantly influences the total modeled

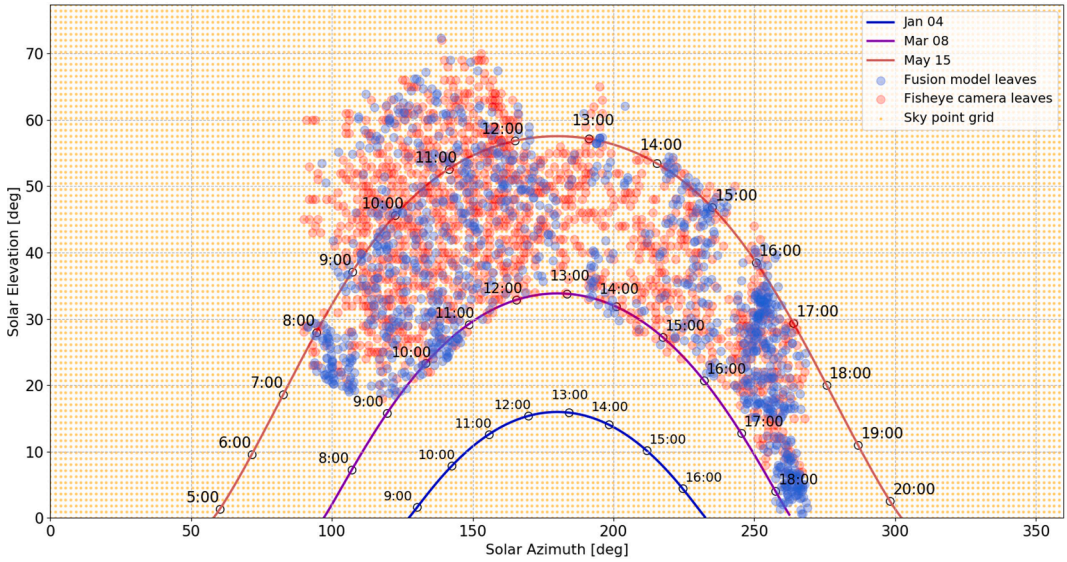


**Fig. C1.** Generated sky point grid (in light orange) and leaf points for SVM classification. (For interpretation of the references to color in this figure legend, the reader is referred to the web version of this article.)

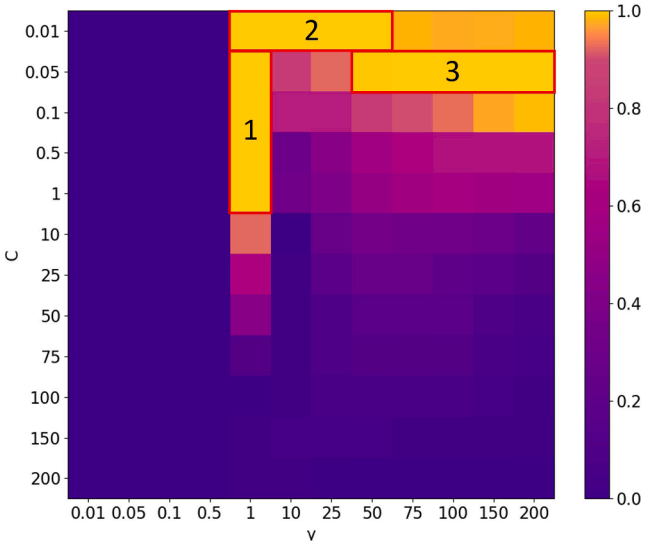


**Fig. C2.** Score matrix of the grid search SVM parameter determination.

irradiance, leading to higher model outputs relative to the measurements. Therefore, the evening discrepancy is attributed to this overestimation of albedo reflections from the west. These albedo reflection-related discrepancies are emphasized in orange in Fig. 22a.

For the discrepancy (in green) between 8:30–9:00 (Index 2) and the one between 16:30–17:00 (Index 7), it can be observed in Fig. 22a that during these time periods, the solar path is obstructed by leaves in the fusion model, while in reality, it is not obstructed by trees (as evidenced by the fisheye photo). Consequently, the fusion model results presented in Fig. 22b are significantly lower than the measured values. Upon examining Fig. 21, it is apparent that this incongruity in leaf area may be attributed to the shedding of branches during tree growth. Since the tree point clouds in our fusion model were collected in 2017, changes in tree morphology over time have not been accounted for, leading to the discrepancies.

Regarding the observed discrepancies between 9:00–10:00 (Index 3) and 14:00–15:00 (Index 6), as depicted in blue, the solar path in Fig. 22a is obstructed by both sets of trees, yet the values simulated by the fusion model in Fig. 22b are notably lower than the measured data. The primary cause of this inconsistency can be attributed to an excessive leaf point density in the LiDAR-collected tree data, an issue known as the multiple return effect, which has been thoroughly investigated in [75]. This increased leaf point density results in an overestimation of the tree shading ratio within the sky segment where the sun is positioned, subsequently leading to underestimations of solar irradiance.

During the two remaining discrepancies (in grey), situated between 10:00–11:00 (Index 4) and 13:00–13:30 (Index 5), Fig. 22a illustrates that the solar path traverses the region collectively shaded by both sets of trees. However, the irradiance data in Fig. 22b during the corresponding periods appear to be predominantly overestimated. This overestimation can also be attributed to tree growth, which results in a lower leaf point density at specific positions in the previously collected point clouds, compared to the actual values, as illustrated in Fig. 21. The lower leaf point density causes the calculated tree shading ratio of the sky segments near the solar position to be lower than the actual ones, eventually resulting in overestimations of irradiance.

As for the discrepancies observed in the results for May 22 in Fig. 23, the underlying causes are fundamentally similar to those identified for May 15. Discrepancies associated with indices 1 and 8 can be attributed to the underestimation and overestimation of albedo reflection, respectively. Discrepancies at indices 2 and 6 arise from the solar path being obstructed by tree branches in the fusion model, even though they are absent in reality. The discrepancy at index 3 stems from the lower leaf point density in the fusion model's corresponding position compared to the actual value, leading to a reduced tree shading ratio. In contrast, discrepancies with indices 4 and 5 are a consequence of the multiple return effect, which causes the local leaf point density to be higher than the real value, resulting in an overestimated tree shading ratio. Finally, it is worth mentioning that the discrepancy with index 7 (highlighted in red) between 17:00 and 17:30 is caused by the fact that the local tree shading area is smaller than the actual size, so the fusion model fails to simulate the shading impacts during this time, resulting in the overestimation of irradiance in Fig. 23b.

In summary, our analysis reveals that the primary source of uncertainty in the hybrid modeling method stems from mismatches between the actual tree morphologies and their representations in the point cloud, which arise due to tree growth. Additionally, albedo reflections in complex urban environments and the multiple return effect during LiDAR point cloud collection further contribute to the inevitable errors in the simulation.

### 4.2. Significance

In the present study, we observed substantial variations in irradiance calculation results across diverse tree modeling approaches. Comparing the high temporal resolution simulation results to the measured data, we found that the fusion model notably surpasses the performance of other models. Thereby the primary significance of the present study is providing an advanced method for accurately predicting tree partial shading impacts in solar irradiance or PV performance modeling.

Additionally, the second key significance is the high scalability of our fusion model-based method, which utilizes readily available urban point clouds as input while minimizing human intervention. Our experiments demonstrate effective integration between the DGCNN segmentation model, surface reconstruction algorithm, and matrix-based irradiance calculation. This automated workflow allows the method to be applicable for simulations across various scales and regions.

Furthermore, the proposed fusion model based method can significantly strengthen the linkage between building performance simulation (BPS) tools and detailed solar irradiance simulation. In particular, the accurate irradiance data obtained by the fusion model can be directly utilized in building-integrated PV (BIPV) system studies and broader building energy system simulations [76]. The tree shading ratio derived from the irradiance calculation can replace the built-in shading module in EnergyPlus, thereby increasing the accuracy of cooling/heating load and solar shading system simulations [77]. Furthermore, the fusion model's capability of automatically reconstructing building geometry simplifies the preparation of BPS simulations by converting the geometry into file formats compatible with BPS tools, such as IDF for EnergyPlus and gbXML for DesignBuilder.

### 4.3. Limitations

Through the in-depth analysis of the major discrepancies between fusion model results and measured data, we determined that tree growth, seasonal defoliation, and regrowth are the primary sources of error. Utilizing point cloud information from previous years may be outdated and can introduce bias. However, the uncertainties present in the LiDAR data employed in this study are deemed acceptable, as the resulting errors in fusion model outputs during the experiments remain significantly smaller than those of other models.

In this study, the impact of tree shading was only simulated during the spring and summer period. Due to the use of fixed point cloud information, the current methodology is only applicable to evergreen tree species and deciduous tree species at specific times. For annual simulations, the defoliation and regrowth characteristics of deciduous species may influence the simulation accuracy to some degree. Therefore, incorporating tree phenology and leaf senescence characteristics of deciduous trees is essential for enhancing the model's performance.

Finally, while examining the major discrepancies, we discovered that the tree shading ratio of sky segments can be overestimated by the multiple return of tree points in the LiDAR sampling process. Consequently, determining how to distinguish and mitigate the multiple return effect during modeling is an issue that future research should address.

### 4.4. Outlook

To address limitations such as tree morphology mismatch between LiDAR data and actual conditions, and the seasonal defoliation and regrowth features of deciduous trees, future research could employ data-driven approaches to interpolate or exclude leaf points, thereby more accurately modeling tree growth behaviors. The recent work by Pan and Jakubiec [2] investigated the seasonal variation of leaves for different deciduous tree species and compiled the data into an open-source database, presenting an opportunity to enhance irradiance simulations involving trees.

Moreover, given that solar irradiance is the most significant factor influencing PV system yield, the accurate irradiance results provided by the fusion model could be integrated with PV performance models in future studies to improve energy generation predictions for urban distributed PV systems subjected to dynamic partial shading impacts.

Additionally, the trained DGCNN model in the present study demonstrates promising performance in semantically segmenting (identifying) objects within urban point clouds. Its potential could be further explored in follow-up research, such as assigning different ground albedo values to various regions based on segmentation results, thus mitigating errors caused by albedo reflection in simulation results, as previously analyzed.

## 5. Conclusion

In this study, we introduce the concept of fusion model as a novel representation of complex urban environments and propose an associated workflow for accurate solar irradiance prediction under partial shading impacts of trees. Our fusion model-based method demonstrates adequate performance in high temporal resolution irradiance prediction experiments, indicating that local transmission features of trees and surrounding reflections play a crucial role in modeling dynamic shading impacts of trees. Compared to other representative models, the fusion model results in significantly lower simulation errors. For the two clear spring days we examined, the relative error differences between the fusion model and the worst case reach up to 80% and 78%, respectively. For long-term modeling, the differences in SEF under clear sky and overcast sky conditions amount to 10.9% and 3.8%, respectively.

Furthermore, we discovered that sky conditions have a considerable impact on irradiance modeling performance, with calculation accuracy under clear skies being notably higher than under overcast skies. Therefore, when conducting simulations under overcast sky conditions, the uncertainties embedded in the results should be considered with additional caution.

The presented workflow offers high scalability, enabling automated irradiance simulations at different scales, such as performing solar assessment for individual buildings or large urban areas using only point cloud data as input. The fusion model based method is expected to effectively inform decision-making for sustainable building design and urban planning by comprehensively accounting for solar resources in cities. Additionally, our method presents the potential to enhance the collaboration between BPS and detailed solar irradiance modeling. By providing more accurate irradiance data, improvements in the accuracy and effectiveness of BPS and building-integrated PV (BIPV) systems modeling tools can be expected in the future.

## Declaration of Competing Interest

The authors declare that they have no known competing financial interests or personal relationships that could have appeared to influence the work reported in this paper.

## Data availability

Data will be made available on request.

## Acknowledgments

The present work is sponsored by the scholarship from China Scholarship Council (CSC, 202107720038).

## Appendix A

### A.1 Radiance matrix-based method

Radiance is arguably the most prevalent tool utilizing matrix-based methods for solar irradiation and daylight simulations in state-of-the-art research. Radiance matrix-based calculation involves three major steps.

*Discretized sky generation*. A discretized sky is a numerical approximation of a continuous sky model [55], expressed by dividing the hemispherical sky dome into multiple segments. Radiance's default is to use the Reinhart division method for sky discretization [78], which is the most common discretization for matrix-based daylight calculation. Fig. A1 shows an example of a discretized sky hemisphere.

*Sky radiance matrix generation*. Radiance adopts the well-known Perez all-weather sky model that considers both direct and diffuse irradiance based on data from the input weather file, and distributes this across the discretized sky hemisphere. The output is a matrix that records the radiance values of each sky segment, as so-called sky radiance matrix. At each timestep of the simulation, a different sky radiance matrix is used to incorporate the effect of changing sun position and weather conditions.

*Daylight coefficient matrix calculation*. The daylight coefficient describes the flux-transfer relation between a luminous sky segment and a sensor point [56]. By using a backward raytracing technique, Radiance is able to quantify the coefficient between the sensor point to each sky segments, and finally form a daylight coefficient matrix [55]. Readers can refer to [52] for more detailed description of the raytracing operation.

By multiplying the daylight coefficient matrix with the sky radiance matrix, the irradiance contribution of each sky segment to the sensor points can be calculated. The final incident irradiance can be derived by summing up the irradiance contributions of all sky segments.

### A.2. Pyrano matrix-based method

Different to the Radiance matrix-based method that takes a model with solid surfaces as input, the Pyrano matrix-based method directly performs daylight calculation based on LiDAR point cloud data. Benefiting from the detailed environmental information provided by the point cloud, Pyrano can take most of the surrounding obstructions into account to preserve sufficient accuracy in the calculation results.

Pyrano's simulation also necessitates the generation of sky radiance matrix based on the discretized sky hemisphere. However, for the calculation of daylight coefficient matrix, instead of ray tracing, Pyrano implements the computational point projection method, which involves three main steps: (1) Calculate analytical daylight coefficient matrix for an empty scene; (2) Calculate cover ratio matrix of the sky segments based on projecting the point cloud onto the sky hemisphere, which expresses the ratio of a certain sky segment area blocked by the obstructions. An example for cover ratio calculation is shown in Fig. A2; (3) Calculate the contribution ratio of sky segments to the received reflected irradiance and combine them with the daylight coefficient matrix as incremental values.

The final daylight coefficient matrix is obtained by multiplying the analytical daylight coefficient matrix with the cover ratio matrix, and then adding the reflection contribution ratio to the calculated values. The subsequent irradiance calculation process is identical to that of Radiance, involving the multiplication of the daylight coefficient matrix with the sky irradiance matrix and the summation of the values within the output matrix. For a more comprehensive description of analytical daylight coefficient and cover ratio calculation procedures, readers can refer to [52].

### A.3. Canopy local transmittance modeling by Pyrano

A characteristic benefit of the Pyrano matrix-based method is its ability to model the semi-transparent properties of trees. Since it first projects the point cloud onto the sky hemisphere, then determines the corresponding cover ratio based on the point sparsity in each sky segment, and ultimately obtains the daylight coefficient between that sky segment and the sensor point. In urban point clouds, tree canopy points are non-uniformly distributed: denser foliage areas with limited solar irradiation penetration have closely spaced points, while sparser foliage areas with greater irradiation penetration have more widely dispersed points. Consequently, when tree points are projected onto the sky, fewer points will be found in the sky segments corresponding to sparser foliage areas, resulting in a smaller cover ratio. Conversely, more points will appear in the sky segments corresponding to denser foliage areas, yielding a larger calculated cover ratio.

Fig. A3 illustrates the estimations of shading impacts from standalone tree canopies on a nearby ground sensor point using different matrix-based methods. As depicted in Fig. A3a, Radiance treats the trees as completely opaque, resulting in minimal contributions from sky segments obstructed by the trees to the irradiance received at the sensor point (shown in full black). Conversely, Fig. A.3b demonstrates that Pyrano allows some sky segments behind the trees to maintain high daylight coefficients (outlined by red dashed line). This indicates that the irradiance from these segments can penetrate the tree canopy and reach the sensor point.

### A.4. Differences in simulation workflow

Building upon the preceding discussion, Fig. A4 provides a schematic representation that delineates the differences between the solar irradiance calculation workflows for the Radiance matrix-based method and the Pyrano matrix-based method.

## Appendix B

### B.1 Pyranometer technical information

| | |
|---|---|
| Usage | Façade irradiance measurement for validation |
| Manufacturer | Kipp & Zonen |
| Pyranometer model | CMP 11 |
| Serial number | 101,399 |
| Sensitivity | 8.68 μV/W/m$^2$ |
| Impedance | 30 Ohm |
| Temperature | 22 ± 2 ℃ |
| Calibration date | February 02, 2010 |

## Appendix C

### C.1 SVM leaf shading area prediction

Support Vector Machine (SVM) is a supervised learning algorithm employed for both classification and regression tasks. It constructs an optimal hyperplane that maximizes the margin between classes to effectively separate data points [74]. Owing to its robust generalization capability and proficiency in handling high-dimensional data, SVM has become prevalent in point set classification.

In this study, we implemented SVM for predicting the leaf shading area by generating a uniformly dense point grid representing the open sky. This grid had azimuth-axis intervals and elevation-axis intervals of 1.8 and 0.9 degrees, respectively, and was positioned behind the two sets of projected leaf points (Fig. C1). Subsequently, SVM was applied to classify sky points as either inside or outside the shading area created by the leaf points within both the fusion model and the fisheye photo.

The Radial Basis Function (RBF) is used as the kernel of the SVM classifier, which is implemented in the Scikit-learn Python package [79]. This RBF kernel facilitates non-linear soft-margin classification, with the performance predominantly governed by two parameters: $C$ and $\gamma$. The parameter $C$ manages the soft-margin cost function, enabling adjustment of the trade-off between misclassifying training data points and creating an overfitted decision surface. Meanwhile, $\gamma$ defines the radius of influence a training point has on the SVM model, with smaller values of $\gamma$ lead to more distinct, localized class boundaries.

In order to determine the optimal $C$ and $\gamma$ values for SVM classification, we employed a grid search method. This involved dividing each leaf point dataset into 10 smaller subsets (folds) and iteratively training the SVM model on nine of the folds using a specified parameter set [$C$, $\gamma$], before testing the model on the remaining fold. $C$ and $\gamma$ values were considered in a range from 0.01 to 200.

The scoring metric for the grid search in this study was calculated based on recall and precision values, as introduced in Section 2.1.2. The scoring formula is provided in Equation (C.1), where $m$ represents the number of datasets (equal to 2) and $n$ denotes the number of folds in the grid search (10 in this case); the $W_{rc}$ and $W_{pc}$ are the weights assigned to recall and precision, respectively. Given the task requirement for the classifier to accurately outline all leaf points while minimizing the misclassification of negative sky points as positive, both $W_{rc}$ and $W_{pc}$ were assigned a value of 0.5.

$$Score = \frac{\sum_{i=1}^{m}\sum_{j=1}^{n}\left(recall \bullet W_{rc} + precision \bullet W_{pc}\right)}{m \times n} \tag{C.1}$$

The grid search results are illustrated in Fig. C2, revealing that the optimal performing SVM model can be trained using [$C$, $\gamma$] sets within three distinct regions: (1) with $\gamma$ set to 1 and $C$ ranging between 0.05 and 1, (2) with $C$ set to 0.01 and $\gamma$ ranging between 1 and 50, and (3) with $C$ set to 0.05 and $\gamma$ ranging between 50 and 200. Based on these findings, the parameter values $C = 0.05$ and $\gamma = 75$ were selected for predicting the final leaf shading area in the present study.

## References


[1] K.D. Coder, Identified benefits of community trees & forests, University of Georgia, 2011.

[2] J. Pan, J.A. Jakubiec, Simulating the Impact of Deciduous Trees on Energy, Daylight, and Visual Comfort: Impact Analysis and a Practical Framework for Implementation. ESIM 2022: Simulation Buildings for the New Normal, Ottawa, Canada, 2022.

[3] A.A. Balogun, T.E. Morakinyo, O.B. Adegun, Effect of tree-shading on energy demand of two similar buildings, Energy Build. 81 (2014) 305–315, https://doi.org/10.1016/j.enbuild.2014.05.046.

[4] Z.-H. Wang, X. Zhao, J. Yang, J. Song, Cooling and energy saving potentials of shade trees and urban lawns in a desert city, Appl. Energy 161 (2016) 437–444, https://doi.org/10.1016/j.apenergy.2015.10.047.

[5] C.-M. Hsieh, J.-J. Li, L. Zhang, B. Schwegler, Effects of tree shading and transpiration on building cooling energy use, Energy Build. 159 (2018) 382–397, https://doi.org/10.1016/j.enbuild.2017.10.045.

[6] S. Zhu, F. Causone, N. Gao, Y. Ye, X. Jin, X. Zhou, X. Shi, Numerical simulation to assess the impact of urban green infrastructure on building energy use: A review, Build. Environ. 228 (2023), 109832, https://doi.org/10.1016/j.buildenv.2022.109832.

[7] R. Compagnon, Solar and daylight availability in the urban fabric, Energy Build. 36 (2004) 321–328, https://doi.org/10.1016/j.enbuild.2004.01.009.

[8] N. Nasrollahi, E. Shokri, Daylight illuminance in urban environments for visual comfort and energy performance, Renew. Sustain. Energy Rev. 66 (2016) 861–874, https://doi.org/10.1016/j.rser.2016.08.052.

[9] M. Rouhollahi, D. Whaley, J. Byrne, J. Boland, Potential residential tree arrangement to optimise dwelling energy efficiency, Energy Build. 261 (2022), 111962, https://doi.org/10.1016/j.enbuild.2022.111962.

[10] A.A.A. Gassar, S.H. Cha, Review of geographic information systems-based rooftop solar photovoltaic potential estimation approaches at urban scales, Appl. Energy 291 (2021), 116817, https://doi.org/10.1016/j.apenergy.2021.116817.

[11] B. Tian, R.C.G.M. Loonen, Á. Bognár, J.L.M. Hensen, Impacts of surface model generation approaches on raytracing-based solar potential estimation in urban areas, Renew. Energy 198 (2022) 804–824, https://doi.org/10.1016/j.renene.2022.08.095.

[12] N. Belhaouas, M.-S.-A. Cheikh, P. Agathoklis, M.-R. Oularbi, B. Amrouche, K. Sedraoui, N. Djilali, PV array power output maximization under partial shading using new shifted PV array arrangements, Appl. Energy 187 (2017) 326–337, https://doi.org/10.1016/j.apenergy.2016.11.038.

[13] B. Meng, R.C.G.M. Loonen, J.L.M. Hensen, Data-driven inference of unknown tilt and azimuth of distributed PV systems, Sol. Energy 211 (2020) 418–432, https://doi.org/10.1016/j.solener.2020.09.077.

[14] Á. Bognár, PV in Urban Context: Modeling and Simulation Strategies for Analyzing the Performance of Shaded PV Systems, Eindhoven University of Technology, 2021.

[15] B. Meng, R.C.G.M. Loonen, J.L.M. Hensen, Performance variability and implications for yield prediction of rooftop PV systems – Analysis of 246 identical systems, Appl. Energy 322 (2022), 119550, https://doi.org/10.1016/j.apenergy.2022.119550.

[16] D. Giaffreda, M. Omaña, D. Rossi, C. Metra, Model for Thermal Behavior of Shaded Photovoltaic Cells under Hot-Spot Condition, in, in: IEEE International Symposium on Defect and Fault Tolerance in VLSI and Nanotechnology Systems, 2011, pp. 252–258, https://doi.org/10.1109/DFT.2011.47.

[17] T.R. Tooke, N.C. Coops, J.A. Voogt, M.J. Meitner, Tree structure influences on rooftop-received solar radiation, Landsc. Urban Plan. 102 (2011) 73–81, https://doi.org/10.1016/j.landurbplan.2011.03.011.

[18] M. Fogl, V. Moudrý, Influence of vegetation canopies on solar potential in urban environments, Appl. Geogr. 66 (2016) 73–80, https://doi.org/10.1016/j.apgeog.2015.11.011.

[19] K. Suomalainen, V. Wang, B. Sharp, Rooftop solar potential based on LiDAR data: Bottom-up assessment at neighbourhood level, Renew. Energy 111 (2017) 463–475, https://doi.org/10.1016/j.renene.2017.04.025.

[20] A. Walch, R. Castello, N. Mohajeri, J.-L. Scartezzini, Big data mining for the estimation of hourly rooftop photovoltaic potential and its uncertainty, Appl. Energy 262 (2020), 114404, https://doi.org/10.1016/j.apenergy.2019.114404.

[21] R. Bohn Reckziegel, E. Larysch, J.P. Sheppard, H.-P. Kahle, C. Morhart, Modelling and Comparing Shading Effects of 3D Tree Structures with Virtual Leaves, Remote Sens. (Basel) 13 (2021) 532, https://doi.org/10.3390/rs13030532.

[22] A. Villalba, A. Pattini, E. Correa, An approach to urban tree daylight permeability simulation using models based on louvers, Build. Environ. 73 (2014) 75–87, https://doi.org/10.1016/j.buildenv.2013.11.026.

[23] J. Konarska, F. Lindberg, A. Larsson, S. Thorsson, B. Holmer, Transmissivity of solar radiation through crowns of single urban trees—application for outdoor thermal comfort modelling, Theor. Appl. Climatol. 117 (2014) 363–376, https://doi.org/10.1007/s00704-013-1000-3.

[24] M. Palme, R. Privitera, D. La Rosa, The shading effects of Green Infrastructure in private residential areas: Building Performance Simulation to support urban planning, Energy Build. 229 (2020), 110531, https://doi.org/10.1016/j.enbuild.2020.110531.

[25] K.A. Al-Sallal, L. Al-Rais, A novel method to model trees for building daylighting simulation using hemispherical photography, J. Build. Perform. Simul. 6 (2013) 38–52, https://doi.org/10.1080/19401493.2012.680496.

[26] R. Berry, S.J. Livesley, L. Aye, Tree canopy shade impacts on solar irradiance received by building walls and their surface temperature, Build. Environ. 69 (2013) 91–100, https://doi.org/10.1016/j.buildenv.2013.07.009.

[27] P. Balakrishnan, J.A. Jakubiec, Trees in Daylight Simulation – Measuring and Modelling Realistic Light Transmittance through Trees, LEUKOS. (2022) 1–28, https://doi.org/10.1080/15502724.2022.2112217.

[28] J.D. Viana-Fons, J. Gonzálvez-Maciá, J. Payá-Herrero, Methodology for the calculation of the shadow factor on roofs and facades of buildings in urban areas, in: XI National and II International Engineering Thermodynamics Congress, Universidad de Castilla-La Mancha José Antonio Almendros Ibáñez, 2019: pp. 870–877.

[29] J.R. Simpson, E.G. McPherson, Simulation of tree shade impacts on residential energy use for space conditioning in Sacramento, Atmos. Environ. 32 (1998) 69–74, https://doi.org/10.1016/S1352-2310(97)00181-7.

[30] J.R. Simpson, Improved estimates of tree-shade effects on residential energy use, Energy Build. 34 (2002) 1067–1076, https://doi.org/10.1016/S0378-7788(02)00028-2.

[31] E.G. McPherson, J.R. Simpson, Potential energy savings in buildings by an urban tree planting programme in California, Urban For. Urban Green. 2 (2003) 73–86, https://doi.org/10.1078/1618-8667-00025.

[32] F. Bernardini, J. Mittleman, H. Rushmeier, C. Silva, G. Taubin, The ball-pivoting algorithm for surface reconstruction, IEEE Trans. Vis. Comput. Graph. 5 (1999) 349–359, https://doi.org/10.1109/2945.817351.

[33] T.K. Dey, J. Sun, An adaptive MLS surface for reconstruction with guarantees, Proceedings of the Third Eurographics Symposium on Geometry Processing. (2005) 43–52.

[34] F. Cazals, J. Giesen, Delaunay triangulation based surface reconstruction, in: J.-D. Boissonnat, M. Teillaud (Eds.), Effective Computational Geometry for Curves and Surfaces, Springer Berlin Heidelberg, 2006, pp. 231–276.

[35] M. Kazhdan, H. Hoppe, Screened poisson surface reconstruction, ACM Trans. Graph. 32 (2013) 29:1-29:13. 10.1145/2487228.2487237.

[36] M. Berger, A. Tagliasacchi, L.M. Seversky, P. Alliez, G. Guennebaud, J.A. Levine, A. Sharf, C.T. Silva, A Survey of Surface Reconstruction from Point Clouds, Comput. Graphics Forum 36 (2017) 301–329, https://doi.org/10.1111/cgf.12802.

[37] J.A. Jakubiec, C.F. Reinhart, A method for predicting city-wide electricity gains from photovoltaic panels based on LiDAR and GIS data combined with hourly Daysim simulations, Sol. Energy 93 (2013) 127–143, https://doi.org/10.1016/j.solener.2013.03.022.

[38] D. Lingfors, J.M. Bright, N.A. Engerer, J. Ahlberg, S. Killinger, J. Widén, Comparing the capability of low- and high-resolution LiDAR data with application to solar resource assessment, roof type classification and shading analysis, Appl. Energy 205 (2017) 1216–1230, https://doi.org/10.1016/j.apenergy.2017.08.045.

[39] D. Lingfors, S. Killinger, N.A. Engerer, J. Widén, J.M. Bright, Identification of PV system shading using a LiDAR-based solar resource assessment model: An evaluation and cross-validation, Sol. Energy 159 (2018) 157–172, https://doi.org/10.1016/j.solener.2017.10.061.

[40] G. Peronato, P. Rastogi, E. Rey, M. Andersen, A toolkit for multi-scale mapping of the solar energy-generation potential of buildings in urban environments under uncertainty, Sol. Energy 173 (2018) 861–874, https://doi.org/10.1016/j.solener.2018.08.017.

[41] Y. Lv, X. Zhang, Y. Liu, 3D modeling of tree crowns and its application in solar energy potential mapping for urban neighborhoods, in, IEEE Geoscience and Remote Sensing Symposium 2014 (2014) 4808–4811, https://doi.org/10.1109/IGARSS.2014.6947570.

[42] M. Münzinger, N. Prechtel, M. Behnisch, Mapping the urban forest in detail: From LiDAR point clouds to 3D tree models, Urban For. Urban Green. 74 (2022), 127637, https://doi.org/10.1016/j.ufug.2022.127637.

[43] X. Zhang, Y. Lv, J. Tian, Y. Pan, An Integrative Approach for Solar Energy Potential Estimation Through 3D Modeling of Buildings and Trees, Can. J. Remote. Sens. 41 (2015) 126–134, https://doi.org/10.1080/07038992.2015.1043004.

[44] F. Szkordilisz, M. Kiss, Passive cooling potential of alley trees and their impact on indoor comfort, Pollack Periodica. 11 (2016) 101–112, https://doi.org/10.1556/606.2016.11.1.10.

[45] W.H. Hwang, P.E. Wiseman, V.A. Thomas, Tree planting configuration influences shade on residential structures in four US cities, Arboriculture & Urban, Forestry 41 (2015) 208–222.

[46] W.H. Hwang, P. Wiseman, V. Thomas, Simulation of Shade Tree Effects on Residential Energy Consumption in Four U.S. Cities, Cities and the Environment (CATE). 9 (2016). https://digitalcommons.lmu.edu/cate/vol9/iss1/2.

[47] G. Peronato, E. Rey, M. Andersen, eds., 3D-modeling of vegetation from LiDAR point clouds and assessment of its impact on façade solar irradiation, The International Archives of the Photogrammetry, Remote Sensing and Spatial Information Sciences. (2016). 10.5194/isprs-archives-XLII-2-W2-67-2016.

[48] Z. Dereli, C. Yücedağ, J.M. Pearce, Simple and low-cost method of planning for tree growth and lifetime effects on solar photovoltaic systems performance, Sol. Energy 95 (2013) 300–307, https://doi.org/10.1016/j.solener.2013.06.019.

[49] R. Levinson, H. Akbari, M. Pomerantz, S. Gupta, Solar access of residential rooftops in four California cities, Sol. Energy 83 (2009) 2120–2135, https://doi.org/10.1016/j.solener.2009.07.016.

[50] A. Jochem, B. Höfle, M. Rutzinger, N. Pfeifer, Automatic Roof Plane Detection and Analysis in Airborne Lidar Point Clouds for Solar Potential Assessment, Sensors 9 (2009) 5241–5262, https://doi.org/10.3390/s90705241.

[51] H.T. Nguyen, J.M. Pearce, Incorporating shading losses in solar photovoltaic potential assessment at the municipal scale, Sol. Energy 86 (2012) 1245–1260, https://doi.org/10.1016/j.solener.2012.01.017.

[52] Á. Bognár, R.C.G.M. Loonen, J.L.M. Hensen, Calculating solar irradiance without shading geometry: a point cloud-based method, J. Build. Perform. Simul. 14 (2021) 480–502, https://doi.org/10.1080/19401493.2021.1971765.

[53] S. Freitas, C. Catita, P. Redweik, M.C. Brito, Modelling solar potential in the urban environment: State-of-the-art review, Renew. Sustain. Energy Rev. 41 (2015) 915–931, https://doi.org/10.1016/j.rser.2014.08.060.

[54] N. Jakica, State-of-the-art review of solar design tools and methods for assessing daylighting and solar potential for building-integrated photovoltaics, Renew. Sustain. Energy Rev. 81 (2018) 1296–1328, https://doi.org/10.1016/j.rser.2017.05.080.

[55] S. Subramaniam, Daylighting simulations with radiance using matrix-based methods, Lawrence Berke-Ley National Laboratory. (2017).

[56] P.R. Tregenza, I.M. Waters, Daylight coefficients, Light. Res. Technol. 15 (2) (1983) 65–71.

[57] M. Inanici, A. Hashemloo, An investigation of the daylighting simulation techniques and sky modeling practices for occupant centric evaluations, Build. Environ. 113 (2017) 220–231, https://doi.org/10.1016/j.buildenv.2016.09.022.

[58] P. Balakrishnan, A. Jakubiec, Measuring light through trees for daylight simulations: A photographic and photometric method, Proceedings of Building Simulation and Optimization. (2016) 1–8.

[59] C.F. Reinhart, O. Walkenhorst, Validation of dynamic RADIANCE-based daylight simulations for a test office with external blinds, Energy Build. 33 (2001) 683–697, https://doi.org/10.1016/S0378-7788(01)00058-5.

[60] Y. Chen, J. Liu, J. Pei, X. Cao, Q. Chen, Y. Jiang, Experimental and simulation study on the performance of daylighting in an industrial building and its energy saving potential, Energy Build. 73 (2014) 184–191, https://doi.org/10.1016/j.enbuild.2014.01.030.

[61] K. Fath, J. Stengel, W. Sprenger, H.R. Wilson, F. Schultmann, T.E. Kuhn, A method for predicting the economic potential of (building-integrated) photovoltaics in urban areas based on hourly Radiance simulations, Sol. Energy 116 (2015) 357–370, https://doi.org/10.1016/j.solener.2015.03.023.

[62] L.O. Grobe, Photon-mapping in Climate-Based Daylight Modelling with High-resolution BSDFs, Energy Build. 205 (2019), 109524, https://doi.org/10.1016/j.enbuild.2019.109524.

[63] 3DBAG, Overview-3D BAG, (2022). https://docs.3dbag.nl/en/ (accessed February 1, 2022).

[64] E. Widyaningrum, Q. Bai, M.K. Fajari, R.C. Lindenbergh, Airborne Laser Scanning Point Cloud Classification Using the DGCNN Deep Learning Method, Remote Sens. (Basel) 13 (2021) 859, https://doi.org/10.3390/rs13050859.

[65] Y. Wang, Y. Sun, Z. Liu, S.E. Sarma, M.M. Bronstein, J.M. Solomon, Dynamic Graph CNN for Learning on Point Clouds, ACM Trans. Graph. 38 (2019) 146:1-146:12. 10.1145/3326362.

[66] A. Diab, R. Kashef, A. Shaker, Deep Learning for LiDAR Point Cloud Classification in Remote Sensing, Sensors 22 (2022) 7868, https://doi.org/10.3390/s22207868.

[67] Kadaster and Geonovum, Publieke Dienstverlening Op de Kaart (PDOK), (n.d.). https://www.pdok.nl/ (accessed November 2, 2022).

[68] S. Raschka, An overview of general performance metrics of binary classifier systems, ArXiv Preprint ArXiv:1410.5330. (2014).

[69] A. Tharwat, Classification assessment methods, Applied Computing and Informatics 17 (1) (2021) 168–192.

[70] TU/e, TNO, SolarBEAT, (2023). https://www.tue.nl/en/research/research-labs/solarbeat (accessed March 30, 2023).

[71] IESNA, IES LM-83-12 IES Spatial Daylight Autonomy (sDA) and Annual Sunlight Exposure (ASE), Technical Report IES LM-83-12 Illuminating Engineering Society of North America. (2012).

[72] W.F. Marion, Ground albedo measurements and modeling, National Renewable Energy Lab.(NREL), Golden, CO (United States), 2019.

[73] J.R.S. Brownson, Chapter 08 - Measure and Estimation of the Solar Resource, in: J. R.S. Brownson (Ed.), Solar Energy Conversion Systems, Academic Press, Boston, 2014, pp. 199–235, https://doi.org/10.1016/B978-0-12-397021-3.00008-9.

[74] C. Cortes, V. Vapnik, Support-vector networks, Mach. Learn. 20 (1995) 273–297.

[75] M. Dalponte, N.C. Coops, L. Bruzzone, D. Gianelle, Analysis on the Use of Multiple Returns LiDAR Data for the Estimation of Tree Stems Volume, IEEE J. Sel. Top. Appl. Earth Obs. Remote Sens. 2 (2009) 310–318, https://doi.org/10.1109/JSTARS.2009.2037523.

[76] C. Lamnatou, J.D. Mondol, D. Chemisana, C. Maurer, Modelling and simulation of Building-Integrated solar thermal systems: Behaviour of the coupled building/system configuration, Renew. Sustain. Energy Rev. 48 (2015) 178–191.

[77] F. Carlucci, R.C.G.M. Loonen, F. Fiorito, J.L.M. Hensen, A novel approach to account for shape-morphing and kinetic shading systems in building energy performance simulations, J. Build. Perform. Simul. 16 (2023) 346–365, https://doi.org/10.1080/19401493.2022.2142294.

[78] A. McNeil, The three-phase method for simulating complex fenestration with radiance, Lawrence Berkley National, Laboratory (2013).

[79] F. Pedregosa, G. Varoquaux, A. Gramfort, V. Michel, B. Thirion, O. Grisel, M. Blondel, P. Prettenhofer, R. Weiss, V. Dubourg, others, Scikit-learn: Machine learning in Python, The, J. Mach. Learn. Res. 12 (2011) 2825–2830.